

AFIT/GE/ENG/04-21



CHARACTERIZATION OF THE TARGET-MOUNT INTERACTION IN
RADAR CROSS SECTION MEASUREMENT CALIBRATIONS

THESIS
Donald W. Powers
Second Lieutenant, USAF

AFIT/GE/ENG/04-21

DEPARTMENT OF THE AIR FORCE
AIR UNIVERSITY

AIR FORCE INSTITUTE OF TECHNOLOGY

Wright-Patterson Air Force Base, Ohio

APPROVED FOR PUBLIC RELEASE; DISTRIBUTION UNLIMITED.

The views expressed in this thesis are those of the author and do not reflect the official policy or position of the United States Air Force, Department of Defense, or the U.S. Government.

AFIT/GE/ENG/04-21

CHARACTERIZATION OF THE TARGET-MOUNT
INTERACTION IN RADAR CROSS SECTION MEASUREMENT
CALIBRATIONS

THESIS

Presented to the Faculty

Department of Electrical and Computer Engineering

Graduate School of Engineering and Management

Air Force Institute of Technology

Air University

Air Education and Training Command

In Partial Fulfillment of the Requirements for the
Degree of Master of Science in Electrical Engineering

Donald W. Powers, B.S.

Second Lieutenant, USAF

March, 2004

APPROVED FOR PUBLIC RELEASE; DISTRIBUTION UNLIMITED.

CHARACTERIZATION OF THE TARGET-MOUNT
INTERACTION IN RADAR CROSS SECTION MEASUREMENT
CALIBRATIONS

Donald W. Powers, B.S.
Second Lieutenant, USAF

Approved:

<u>//SIGNED//</u> Maj William D. Wood, PhD Thesis Advisor, posthumously	<u>12 Mar 04</u> Date
<u>//SIGNED//</u> Dr. Michael Havrilla Committee Member	<u>12 Mar 04</u> Date
<u>//SIGNED//</u> Dr. Kueichien Hill Committee Member	<u>12 Mar 04</u> Date
<u>//SIGNED//</u> Dr. Michael Temple Committee Member	<u>12 Mar 04</u> Date

Acknowledgements

First and foremost, I would like to thank both my parents and my fiancée for supporting me throughout the completion of this challenging endeavor. Often times I made it extremely difficult to even hold a conversation with, but I hope each of you truly understand how much of an impact you have had on me. No words can describe how much I appreciate it.

Next I would like to thank the guys in the microwave lab. John and Pete, you guys were instrumental in the success of this research. From questions concerning research, to the head bopping of the same songs everyday, I can say that you guys made the research process enjoyable.

To all my fellow classmates, thanks for the help throughout the courses. Tom I truly appreciate you taking the time to sit down and explain things when I just wasn't getting it or I just needed someone to talk to! I have to admit, I have to remember to sit aside an extra hour when I call you on the phone.

I would like to also thank my committee Dr. Hill, Dr. Havrilla, and Dr. Temple. I appreciate the direction provided, and I enjoyed working with each of you.

How could I ever forget the two gentlemen who carried me on their backs across the finish line of this marathon. It has been extremely rewarding working with you guys. We were there for one another when times were tough, and we made the best of everything. Chief and Ryan, thanks!

Finally, I would like to dedicate this research in memory of Major William D. Wood. Without his technical expertise and guidance this research would have never come together as a success. Major Wood was truly an outstanding individual that I could call more than just an advisor, he was a friend. He will truly be missed.

Donald W. Powers

Table of Contents

	Page
Acknowledgements	iv
List of Figures	viii
List of Tables	x
List of Abbreviations	xi
Abstract	xii
I. Introduction	1-1
1.1 Problem Defintion	1-1
1.2 Assumptions	1-2
1.3 Thesis Overview	1-4
II. Literature Review and Background Information	2-1
2.1 Significant Contributions and Related Work	2-1
2.1.1 Reduction/Elimination Research Efforts	2-1
2.1.2 Characterization Research Efforts	2-2
2.2 Radar Cross Section Defined	2-2
2.3 Radar Cross Section Measurements Overview	2-4
2.3.1 Clutter Sources and Suppression Techniques	2-6
2.4 Basic Electromagnetic Theory	2-8
2.4.1 Maxwell's Equations	2-8
2.4.2 Vector Potentials	2-10
2.4.3 Scattering	2-14
2.4.4 Surface Equivalence Principle	2-15
2.5 Integral Equation Formulation	2-18
2.5.1 Surface Electric Field Integral Equation	2-18
2.5.2 Surface Magnetic Field Integral Equation	2-22
2.5.3 Surface Combined Field Integral Equation	2-23
2.6 Method of Moments (MoM)	2-24
2.6.1 CARLOS	2-25

	Page
III. Methodology	3-1
3.1 Generalized Isolation Process of the Interaction Scattering Mechanism	3-1
3.2 Proof of Concept: A Simple Two Cylinder Geometry	3-5
3.2.1 Computational Experimental Setup	3-5
3.2.2 RCS Measurement Setup	3-7
3.2.3 Geometric Optics Setup and Approximation	3-8
3.3 Pylon Model and Its Parameters	3-10
3.3.1 Computational Setup for the Pylon-Cylinder Model	3-13
3.3.2 Isolation of the Interaction in the Calibration Target-Mount Configuration	3-14
3.4 “Difference” Currents	3-17
IV. Results and Analysis	4-1
4.1 Two Cylinder Geometry	4-1
4.1.1 Perfect Electric Conductor (PEC) Cylinder 1 and 2 Results	4-1
4.1.2 Combination of Cylinder 1 and 2	4-4
4.1.3 Isolation of the Interaction Between Cylinder 1 and 2	4-6
4.2 Cylinder/Pylon Configuration	4-7
4.2.1 Validation of Hertzian Dipole Approximation	4-8
4.2.2 Results for Calibration Targets	4-9
4.2.3 Cylinder Mounted on Pylon	4-10
4.2.4 Isolation of the Interaction in the Calibration Target-Mount Configuration	4-12
4.2.5 Difference Currents on the Surface of the Calibration Targets	4-14
V. Conclusions and Future Work	5-1
5.1 Conclusions	5-1
5.1.1 Conclusions on Simple Two Cylinder Geometry	5-1
5.1.2 Conclusions on Calibration Target-Mount Configuration	5-1
5.2 Future Work	5-2
Appendix A. Geometric Optics Analysis	A-1
A.1 Single Cylinder Derivation	A-1
A.2 “Double Bounce” Derivation	A-3
A.3 RCS Calculations	A-5
A.3.1 $\vec{E}_{t,m}^s$ RCS Calculation	A-5

	Page
A.3.2 \vec{E}_{int}^s RCS Calculation	A-6
A.3.3 \vec{E}_{tm}^s RCS Calculation	A-6
Bibliography	BIB-1
Vita	VITA-1

List of Figures

Figure		Page
1.1.	Quiet Zone in a RCS Measurement Facility	1-2
2.1.	Physical Interpretation of RCS	2-3
2.2.	Far Field RCS Range with potential clutter sources shown. .	2-7
2.3.	Electromagnetic Illumination of Inhomogeneous Medium . . .	2-9
2.4.	Surface Equivalence Principle	2-14
2.5.	Love's Equivalence Principle	2-16
2.6.	Physical Equivalence Principle	2-17
2.7.	Interior and Exterior Equivalence for a Dielectric Scatterer .	2-19
2.8.	Example Facet file inputed into CARLOS	2-26
3.1.	Flowchart for Isolation of Interaction Scattering Mechanism .	3-4
3.2.	Proof of Concept: Simple Cylinder Geometry	3-6
3.3.	Triangular Meshed Cylinder for CARLOS Input	3-7
3.4.	Pictures of Range Experimental Setup	3-8
3.5.	Two-dimensional view of Simple Cylinder Geometry	3-10
3.6.	Geometry of an Ogive	3-11
3.7.	Geometry of Target-Mount Configuration with two calibration targets	3-14
4.1.	Simple Two Cylinder Geometry Results for Cylinder 1 and 2 Illuminated Separately	4-2
4.2.	Surface Currents on Cylinder 2	4-3
4.3.	Simple Two Cylinder Geometry Results for Cylinder 1 + 2 .	4-4
4.4.	Downrange Image of Two-Cylinder Configuration	4-5
4.5.	Path Length Differences	4-7
4.6.	Simple Cylinder Geometry Results for the Interaction Scatter- ing Mechanism	4-8
4.7.	Validation of Approximation for Far-Field Translation on 1500x350 Calibration Target-Mount Configuration	4-9
4.8.	Validation of Approximation for Far-Field Translation on 1800x1200 Calibration Target-Mount Configuration	4-9
4.9.	Example Calibration Target Mesh	4-10
4.10.	Calibration Target Frequency Sweep Results	4-11
4.11.	Example Meshed Geometry for Calibration Target-Mount Con- figuration	4-12
4.12.	RCS of Both Calibration Target-Mount Configurations	4-13

Figure		Page
4.13.	RCS of the Interaction in the Calibration Target-Mount Configuration	4-14
4.14.	Surface Currents on the 1800x1200 Calibration Target	4-17
4.15.	RCS of Target in the Presence and Absence of the Pylon VV-Pol	4-18
4.16.	Surface Currents on the 1800x1200 Calibration Target	4-19
4.17.	RCS of Target in the Presence and Absence of the Pylon HH-Pol	4-20
A.1.	Single Cylinder Geometry	A-1
A.2.	Two-Cylinder Geometry	A-3

List of Tables

Table		Page
2.1.	Summary of Clutter Sources in a RCS Range and Potential Corrections	2-6
3.1.	Ogive Pylon Parameters	3-12
4.1.	Scattering Mechanisms and Downrange Images	4-6

List of Abbreviations

Abbreviation		Page
RCS	Radar Cross Section	1-1
RAM	Radar Absorbing Material	1-1
SNR	Signal-to-Noise Ratio	1-4
MoM	Method of Moments	2-1
CARLOS	<u>C</u> ode for <u>A</u> nalysis of <u>R</u> adiators on <u>L</u> ossy <u>S</u> urfaces	2-1
EFIE	Electric Field Integral Equation	2-8
MFIE	Magnetic Field Integral Equation	2-8
PEC	Perfect Electric Conductor	2-16
PMC	Perfect Magnetic Conductor	2-16
ACAD	Advanced Computer Aided Design	2-26
GO	Geometric Optics	3-8

Abstract

Radar Cross Section (RCS) measurements are quintessential in understanding target scattering phenomenon. The reduced RCS of modern weapons systems stresses the capability of current RCS measurement ranges. A limiting factor that has recently become more significant is the electromagnetic coupling between a test target and the mounting hardware used to support it and control its orientation during the RCS measurement. Equally important is the electromagnetic coupling between the RCS calibration artifact and its mount, which provides an opportunity to explore the coupling phenomena without delving into operationally sensitive areas.

The primary research goal was to characterize the interaction between a calibration artifact and its mounting apparatus when measuring the RCS of the calibration artifact as part of a larger RCS measurement process. Standard methods, such as vector background subtraction, do not account for this interaction. By understanding the interaction term, a more accurate measurement of target RCS may be obtained. Through careful characterization of the interaction, an additional term can be included in the vector background subtraction equation to reduce the level of uncertainty.

Two techniques were developed to isolate and characterize the interaction between the target and mount. The first involves evaluating the far-zone fields scattered by the target under two conditions: the target alone and then the target with mounting hardware present. The fields are then coherently subtracted to isolate the interaction. This process was validated with measurements and computational results. The second technique involves evaluating fields on the target surface under the aforementioned conditions, which are subsequently subtracted from one another

and radiated to the far-field. The advantages and disadvantages of each technique are investigated.

Results for twin-cylinder and cylinder/pylon configurations are presented. Validation is achieved through comparison with physical measurements. Results indicate the target-mount interaction is most significant at low frequencies.

CHARACTERIZATION OF THE TARGET-MOUNT INTERACTION IN RADAR CROSS SECTION MEASUREMENT CALIBRATIONS

I. Introduction

Radar Cross Section (RCS) measurements are quintessential in understanding target scattering phenomenon. By determining the scattering centers of a target, major scattering contributions can be obtained. Such contributions can then be reduced by the application of surface treatments, such as Radar Absorbing Materials (RAM). Due to the significant contributions in the reduction of RCS signatures, contributions other than those from the target have become increasingly important to characterize/eliminate due to the demand of highly accurate measurements. Highly accurate measurements are needed to determine the survivability of an aircraft. How susceptible is a target to a threat radar? How large are the signature contributions from certain aspects of the aircraft? Questions like these need to be answered, but without accurate measurements, the answer is unknown or inaccurate.

1.1 Problem Definition

In any measurement system, the measurements obtained are no more accurate than the calibration taken. The primary goal of this research is to characterize the interaction between a calibration target and mounting apparatus (e.g. forward canted ogive cross-section pylon) when measuring the RCS of a target. Currently, the methods employed (vector background subtraction) do not account for this interaction, therefore, by characterizing the interaction term, a more accurate measurement of the target's RCS can be obtained. By characterizing the interaction, an additional

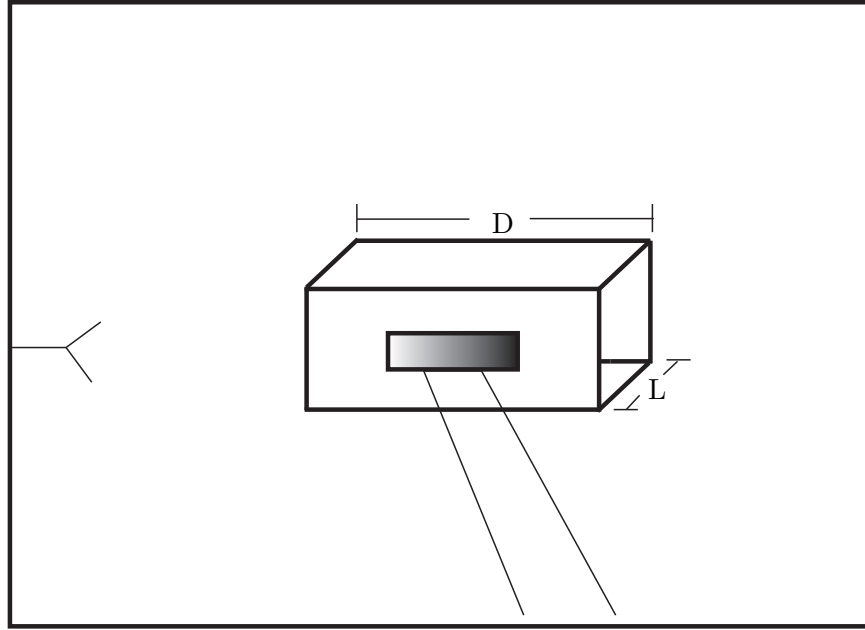


Figure 1.1: The quiet zone in a RCS measurement facility. The downrange extent is based on a variation in amplitude of 1 dB and the crossrange extent on a $\frac{\pi}{8}$ phase variation.

term can be included in the vector background subtraction equation to eliminate another level of uncertainty.

1.2 Assumptions

The following section will describe the assumptions used to create the model and an explanation as to why each assumption can be made. The assumptions here will apply to the model described in Chapter III and the computational results in Chapter IV. The first assumption to be discussed is the far-field requirement. In any RCS measurement facility there is a region, defined as the *quiet zone*, in which the plane-wave excitation is approximately uniformly planar. A planar wavefront is defined as a wavefront having planar equiphase and equiamplitude surfaces [1]. Typically, the limits of the amplitude and phase variations of a quiet zone are defined such that the variation in amplitude is no more than 1 dB in the downrange extent, and a maximum phase variation of $\frac{\pi}{8}$ in the crossrange extent. Although these limits

tolerances are arbitrary, they are widely accepted. The downrange dimension, D , of a quiet zone for a far-field range, using the previous limits is defined by [2],

$$D \approx \frac{R}{8.2}, \quad (1.1)$$

where R is the distance from the radar to a common reference point on the target, respectively. Similarly, the cross range dimension of a quiet zone utilizing the previous measurement tolerances is defined by [2],

$$L = \sqrt{\frac{cR}{2f}}, \quad (1.2)$$

where L is the cross range dimension, c is the speed of light, R is the distance from the radar to a common reference point on the target, and f is the frequency. Another way to envision the quiet zone is by a 3-dimensional box with dimensions L and D depicted in Fig. 1.1. Outside this region, the amplitude and phase variations do not meet the far-field requirement. That is, the incident field is no longer a uniform plane wave. Therefore, caution must be used when modelling portions of the mount outside the quiet zone region. Within the computational model, it is difficult to accurately model the returns from a spherical wavefront on the lower portion of the mount, therefore, returns from the lower portion of the mount must be mitigated. This can be accomplished by placing impedance surface treatments on the lower portion of the ogive mount. This model more closely resembles the measurement setup since returns outside the quiet zone are excluded through hardware range gating, which will be discussed in greater detail in Chapter II. Additionally, the model created is illuminated by plane-waves.

Another assumption to the model is the clutter will be considered negligible. In the computational portion of this research the data obtained is noiseless, which is comparable to the measurements taken in practice, using pulse integration. Both vector background subtraction and hardware range gating help to eliminate

the clutter associated with the range, while pulse integration, helps to increase the Signal-to-Noise Ratio (SNR).

1.3 Thesis Overview

The following section will provide a brief outline and overview of what each chapter consists of.

Chapter II provides the reader with the background information pertaining to previous work in the field of characterizing and eliminating the interaction, electromagnetic scattering theory, and a brief overview of the three-dimensional Method of Moments code, CARLOS.

Chapter III provides the reader with the methodology on the two isolation/characterization processes.

Chapter IV will discuss results on the two isolation/characterization process described in Chapter III

Chapter V will provide a conclusion based on the analysis performed in Chapter IV and potential future work in the area of characterizing the interaction term.

Again, the goal of this research is to characterize the interaction between a calibration object and mount in a RCS measurement and apply this interaction to the vector background subtraction equation and obtain a modified version that takes the form:

$$\sigma_{tgt} = \frac{|\vec{E}_{tgt}^s - \vec{E}_{bkg}^s|^2}{|\vec{E}_{cal}^s - \vec{E}_{cbk}^s - \vec{E}_{cint}^s|^2} \sigma_{cal} \quad (1.3)$$

This research provides another piece to the characterization of the interaction puzzle, however, the ultimate goal is to provide an additional term (\vec{E}_t^{sint}) to the

numerator of the vector background subtraction equation to account for the “true” target and mount interaction. Future research will be discussed in Chapter V.

By modeling and characterizing the effects of the interaction, which is considered a low-level source of contamination, can be useful in the sense that it can answer certain questions about the measurements. That is, when can the interaction be ignored, or even more importantly when does one need to apply the interaction term in the modified vector background subtraction equation? Questions like these will be answered in the following research.

II. Literature Review and Background Information

The primary objective of this chapter is to discuss the work that has been accomplished in the past in relation to the characterization or reduction of the interaction term, and the theory necessary to properly utilize the tools to characterize the interaction term. In particular, the concept of Radar Cross Section, and how measurements are currently taken will be explained. Moreover, basic electromagnetic scattering theory will be described up to the formulation of the integral equations to describe what the three-dimensional Method of Moments MoM code, CARLOS, ultimately solves for. By providing a brief overview of these important concepts, the goal of determining how to characterize the interaction and why the characterization of the interaction term is necessary for accurate measurements will become evident.

2.1 Significant Contributions and Related Work

Minimal research in the area of characterizing the interaction between a calibration target and mount has been previously conducted. However, a considerable amount of research has been conducted in the area of reducing or eliminating the interaction between the target and the mount. The following sections will describe the research efforts in the areas of reduction/elimination and characterization of the interaction between the target and the mount.

2.1.1 Reduction/Elimination Research Efforts. As previously mentioned, the reduction or elimination of the interaction between the target and mount has been the primary area of research pertaining to the interaction term in the RCS community. In particular, work done by Berrie and Wilson in the area of designing support columns constructed out of Expanded Poly-Styrene (EPS) foam [3]. This work involved numerical simulations and validations through measurements. Another area of research in the removal of the interaction has also been accomplished by LaHaie, et. al, using processing techniques on RCS measurements [4].

This technique involved image editing on data that had been preprocessed utilizing cross-calibration between numerical and measured data and stationary background removal. The research in effect showed an improvement in the RCS of the target under consideration, but ultimately there were still levels of inaccuracy.

2.1.2 Characterization Research Efforts. Work in the realm of characterizing the interaction between the target and mount has been accomplished, but kept to a minimum. One piece of work by Burns et. al, in particular, takes a look at numerical and measured results to show that the measured results are in very close agreement with the perturbations caused from the target and mount [5]. The data shows that there is some form of interaction, which can be attributed to the electromagnetic coupling of the target and the mount, and such observations will be used to develop post-processing techniques to mitigate the interaction.

As stated previously, very little work has been done in the area of characterizing the interaction between calibration targets and the mounts utilized in RCS measurements. The research efforts carried out in this paper, will provide an interaction term that can be utilized to modify the vector background subtraction equation, in hopes of obtaining a more accurate representation of a target's radar cross section, especially when the target is of low cross section.

2.2 Radar Cross Section Defined

Consider the situation in Figure 2.1 [2]. Assuming that the target is at a great distance from the radar, the incident wave can be considered uniformly planar with incident power flux, P_i in $\frac{W}{m^2}$. Now, consider the target to have hypothetical some capture area, σ . Due to this capture area, the target captures σP_i watts of energy. Finally, the target radiates the captured energy isotropically over 4π steradians, thereby the scattered power density at a distance R (considered large)

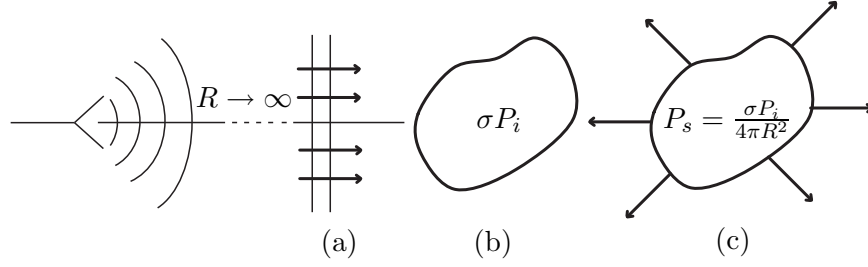


Figure 2.1: (a) Planar wave fronts with incident power flux P_i . (b) Target with “capture area” σ which captures σP_i of energy. (c) Target then reradiates “captured energy” equally in all directions (isotropically).

can be written

$$P_s = \frac{\sigma P_i}{4\pi R^2} \quad (2.1)$$

Radar Cross Section, σ , can be formally defined as the area of a perfect reflector of electromagnetic waves that would reflect the equivalent amount of energy back to the radar as would the hypothetical target [2]. As described previously, using the situation in Fig. 2.1 and rearranging Eqn. (2.1), the RCS of the target can be described mathematically as,

$$\sigma = \lim_{R \rightarrow \infty} 4\pi R^2 \frac{P_s}{P_i}. \quad (2.2)$$

Traditionally, though, it is more convenient to express the RCS in terms of the electric field. This can be accomplished by noting fact that the power density of an electromagnetic wave is proportional to the magnitude squared of the electric field [2]. Therefore Eqn. (2.2) can be rewritten in the form,

$$\sigma = \lim_{R \rightarrow \infty} 4\pi R^2 \frac{|\vec{E}^s|^2}{|\vec{E}^i|^2}, \quad (2.3)$$

where \vec{E}^s is the scattered electric field at the receiver, and \vec{E}^i is the incident electric field at the target. For Eqn. (2.3) to hold the target is considered to be at a great

distance from the radar ($R \rightarrow \infty$) such that the incident wave is locally uniformly planar and not spherical.

RCS, typically measured in square meters (m^2), may mislead one into believing that the RCS of a target is just the measure of the physical projected area of the target. However, RCS is actually a function of many other parameters. RCS is a function of [2]:

- target geometry and material composition
- angular orientation of target relative to transmitter and receiver
- frequency or wavelength;
- transmitter polarization;
- receiver polarization.

2.3 Radar Cross Section Measurements Overview

In most measurement systems a calibration is paramount in obtaining accurate measurements. This, too, holds for RCS measurements. Typically measurements are taken in which a target and a calibration object (sphere, squat cylinder, etc.) are sequentially illuminated and the signal received from each is recorded. By doing so, and utilizing the exact solution for the calibration object, the RCS of the target can be related to the calibration object [2]. Mathematically this is represented by,

$$\sigma_{tgt} = \frac{P_{tgt}}{P_{cal}} \sigma_{cal}, \quad (2.4)$$

where σ_{tgt} and σ_{cal} are the RCS of the target and calibration object, respectively, and P_{tgt} and P_{cal} are the power received from the target and calibration object, respectively. Again, utilizing the fact that the power density of an electromagnetic wave is proportional to the magnitude squared of the electric field, Eqn. (2.4), can

be rewritten as,

$$\sigma_{tgt} = \frac{|\vec{E}_{tgt}^s|^2}{|\vec{E}_{cal}^s|^2} \sigma_{cal}, \quad (2.5)$$

where \vec{E}_{tgt}^s and \vec{E}_{cal}^s are the scattered electric fields for the target and calibration object, respectively. To obtain a more accurate measurement of the RCS of a target, vector background subtraction can be utilized to eliminate clutter sources associated with the range and the target support hardware. To utilize vector background subtraction additional measurements must be made, and Eqn. (2.5) must be modified to account for the additional measurements. The modified equation is

$$\sigma_{tgt} = \frac{|\vec{E}_{tgt}^s - \vec{E}_{bkg}^s|^2}{|\vec{E}_{cal}^s - \vec{E}_{cbk}^s|^2} \sigma_{cal}, \quad (2.6)$$

where the measurements are:

- \vec{E}_{tgt}^s : Scattered field seen by the receiver when the target is present
- \vec{E}_{bkg}^s : Scattered field seen by the receiver when no target is present, but all other hardware still in place
- \vec{E}_{cal}^s : Scattered field seen by the receiver when the calibration object is present
- \vec{E}_{cbk}^s : Scattered field seen by the receiver when the calibration object is not present, but all other hardware still in place

Since radar and range responses tend to drift with environmental changes the additional measurements should be taken in relatively the same time frame [2]. Although vector background subtraction helps to eliminate clutter due to the chamber, it should be noted that Eqn. (2.6) is not perfect since it does not account for all of the clutter sources in the chamber, specifically, it neglects target-mount interactions. Table 2.1, although not a complete list of clutter sources, summarizes the clutter sources in a RCS range and the possible techniques used for suppression. Additionally, the following section will provide an overview of the current techniques utilized

to suppress the clutter in a RCS range. It should be noted that according to Table 2.1, there are no techniques that characterize/eliminate the interaction between the target and mount.

2.3.1 Clutter Sources and Suppression Techniques. According to Table 2.1, there are several techniques capable of suppressing clutter due to the RCS range. Figure 2.2 depicts a general RCS range with clutter sources indicated. Introduced in Section 2.3, vector background subtraction helps to reduce the clutter due to the back-wall scattering. It however, does not account for other forms of clutter. Therefore, other techniques were devised to suppress other forms of clutter. In particular, hardware range gating was developed to suppress the interactions with target-floor interactions and also to aid in the suppression of the back-wall scattering. Almost as equally important is the use of pulse integration to increase the Signal-to-Noise Ratio, (SNR).

2.3.1.1 Hardware Range Gating. Hardware range gating involves transmitting a signal for some period of time and then turning on the receiver when the anticipated return from the target is expected. This technique is used to suppress the returns from the floor and back-wall scatterers. It is apparent from Fig. 2.2 that the signal that directly reflects off the target will return to the radar in a shorter amount of time than those from the floor and back-wall, based on the distance travelled. The one disadvantage to hardware gating is the case in which either a cavity like target (open cylinder) or the target is in some sort of resonance is

Table 2.1: Potential clutter sources with techniques used to suppress.

Error Sources	Background Subtraction	Hardware Gating	Pulse Averaging
Receiver Noise	No	No	Yes
Back-wall Scattering	Yes	Yes	No
Target/Mount Interaction	No	No	No
Target/Floor Interaction	No	Yes	No

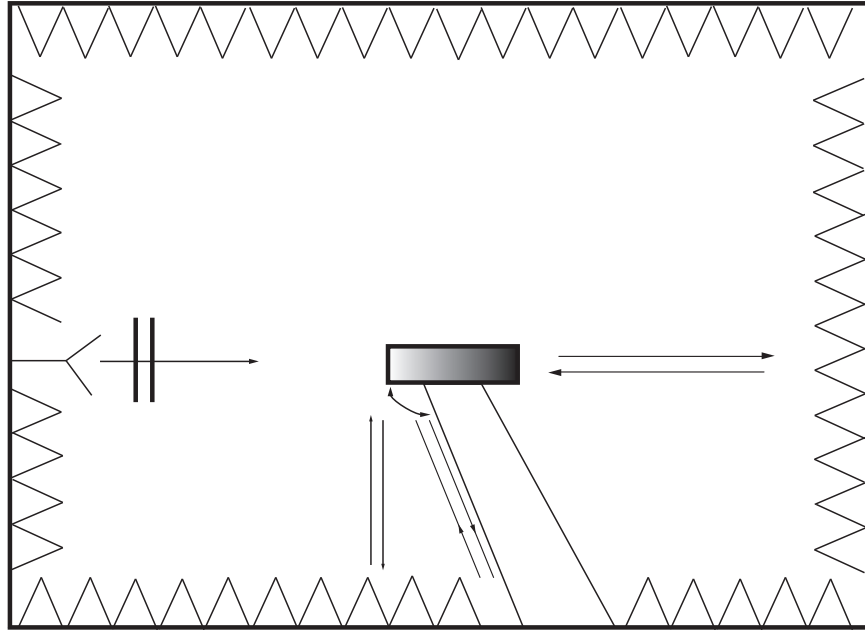


Figure 2.2: An example RCS range with clutter sources shown. All scattering is characterized by the following. The target-floor interaction, target-backwall scattering, and target/mount interaction.

measured. Targets that have these features, typically, have returns that occur later in time, therefore, hardware range gating may exclude the readings back to the receiver [2].

2.3.1.2 Pulse Integration. Pulse integration is a technique utilized to suppress noise in the range. Pulse integration is a process of summing all the available pulses to enhance detection [6]. Pulse integration more or less boosts the signal. There are two types of integration that can be carried out, coherent and incoherent integration. Coherent integration is carried out with phase information preserved, which is discarded in incoherent integration. Another name for coherent and incoherent integration is predetection and post-detection integration, respectively [6]. As one might expect, since coherent integration requires that phase information of the signal be preserved, it is more difficult to accomplish than that of incoherent

integration. However, it will provide a much improved Signal to Noise Ratio, (SNR), than that of its incoherent counterpart.

Ultimately, the point that needs to be addressed is the fact that certain clutter sources occur with or without the presence of the target, however, certain clutter is only present when the target is present i.e. target-mount interaction. Hence, the need for some way of eliminating the interaction between the target and the mount arises.

2.4 Basic Electromagnetic Theory

The development of Radar Cross Section would be incomplete without the introduction of basic electromagnetic scattering theory, the formulation of the Electric and Magnetic Field Integral Equations, EFIE and MFIE , respectively, and the solutions to unknown equivalent current densities which ultimately solve for the scattered fields.

To aid in the understanding of the formulation of the integral equations, a brief summary of basic electromagnetic theory and how it is applied to scattering is provided. Through the development of the Helmholtz wave equation, the use of vector potentials as an intermediate step to the fields produced by a scatterer, and the implementation of the surface equivalence theorem, the integral equations can be formulated.

2.4.1 Maxwell's Equations. Consider a region of space containing an inhomogeneous medium characterized by permittivity, $\epsilon = \epsilon_0\epsilon_r$ and permeability, $\mu = \mu_0\mu_r$, as depicted in Fig. 2.3, illuminated by an electromagnetic field in which both \vec{E} and \vec{H} vary with position on V . The fields in the region of the inhomogeneous, linear and isotropic medium, satisfy Maxwell's equations (utilizing the $e^{j\omega t}$

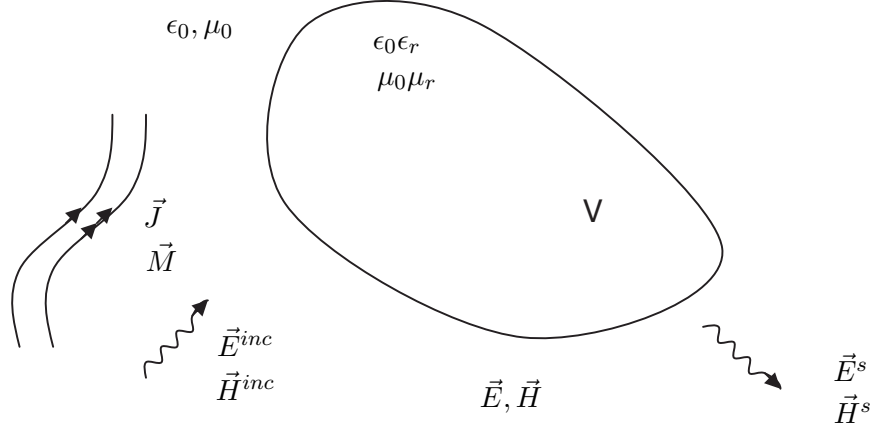


Figure 2.3: Inhomogeneous material illuminated

time convention) [7]:

$$\nabla \times \vec{E} = -j\omega\mu\vec{H} - \vec{M} \quad (2.7)$$

$$\nabla \times \vec{H} = j\omega\epsilon\vec{E} + \vec{J} \quad (2.8)$$

$$\nabla \cdot (\epsilon\vec{E}) = q_{ev} \quad (2.9)$$

$$\nabla \cdot (\mu\vec{H}) = q_{mv} \quad (2.10)$$

where \vec{E} and \vec{H} are the electric and magnetic fields (both of which are a function of position), \vec{J} and \vec{M} are electric and magnetic current densities, and q_{ev} and q_{mv} are the electric and magnetic source charges, respectively. To develop the inhomogeneous wave equations one may start by dividing Faraday's Law, Eqn. (2.7), by μ , followed by a curl operation to both sides of the equation, and substituting Ampere's Law, Eqn. (2.8); the wave equation for the electric field, Eqn. (2.11), is obtained. Through a similar process, except beginning with Ampere's Law, and substituting in Faraday's Law, the magnetic field wave equation, Eqn. (2.12), is obtained. The electric and

magnetic field wave equations for an inhomogeneous medium are:

$$\nabla \times \left[\frac{1}{\mu} \nabla \times \vec{E} \right] - \omega^2 \epsilon \vec{E} = -j\omega \vec{J} - \nabla \times \left[\frac{1}{\mu} \vec{M} \right] \quad (2.11)$$

$$\nabla \times \left[\frac{1}{\epsilon} \nabla \times \vec{H} \right] - \omega^2 \mu \vec{H} = -j\omega \vec{M} + \nabla \times \left[\frac{1}{\epsilon} \vec{J} \right] \quad (2.12)$$

If the material is assumed to be linear, isotropic, and *homogeneous*, then Eqn's. (2.11) and (2.12) simplify to the well known result of:¹

$$\nabla^2 \vec{E} + k^2 \vec{E} = j\omega \mu \vec{J} - \frac{\nabla(\nabla \cdot \vec{J})}{j\omega \epsilon} + \nabla \times \vec{M} \quad (2.13)$$

$$\nabla^2 \vec{H} + k^2 \vec{H} = j\omega \epsilon \vec{M} - \frac{\nabla(\nabla \cdot \vec{M})}{j\omega \mu} - \nabla \times \vec{J} \quad (2.14)$$

Equations (2.13) and (2.14) imply that the electric and magnetic fields satisfy the forced wave equations. Due to the $\nabla \nabla \cdot$ operation, though, solutions to \vec{E} and \vec{H} are difficult to obtain. A classical approach to obtaining the solutions to the forced wave equation is through the use of an intermediate step. Specifically, the step involves the magnetic and electric vector potentials, \vec{A} and \vec{F} , respectively.

2.4.2 Vector Potentials. Vector potentials are considered the intermediate step in determining the electric and magnetic fields. It will be shown that the potential fields will satisfy a simpler (i.e. no $\nabla \nabla \cdot$ operations) vector wave equation, and how they relate to the electric and magnetic fields.

2.4.2.1 Magnetic Vector Potential: \vec{A} and Electric Vector Potential: \vec{F} . Assuming a magnetic source-free region ($\vec{M} = q_{mv}^i = 0, \vec{J} = q_{mv}^i \neq 0$), Gauss' Magnetic Law, Eqn. (2.10), is identically zero. Utilizing the the vector identity $\nabla \cdot (\nabla \times \vec{A}) = 0$ in conjunction with the previous statement, the relationship

¹Use vector identity $\nabla \times \nabla \times \vec{A} = \nabla(\nabla \cdot \vec{A}) - \nabla^2 \vec{A}$ and the continuity equations: $\nabla \cdot \vec{J} = -j\omega q_{ev}$ and $\nabla \cdot \vec{M} = -j\omega q_{mv}$ and $k = \omega \sqrt{\mu \epsilon}$

between \vec{H}_A and \vec{A} is obtained,

$$\vec{H}_A = \frac{1}{\mu} \nabla \times \vec{A}, \quad (2.15)$$

where \vec{H}_A represents the magnetic field due to the vector potential \vec{A} . The electric scalar potential, ϕ_e , is introduced by substituting Eqn. (2.15) into Faraday's Law, Eqn. (2.7), and obtaining a reduced equation in the form:

$$\nabla \times [\vec{E}_A + j\omega\vec{A}] = 0 \quad (2.16)$$

Utilizing another vector identity, $\nabla \times (\nabla\phi_e) = 0$, in conjunction with Eqn. (2.16), the electric scalar potential is defined as:

$$-\nabla\phi_e \doteq \vec{E}_A + j\omega\vec{A} \quad (2.17)$$

Solving for \vec{E}_A in Eqn. (2.17), the relationship between \vec{E}_A and \vec{A} is obtained,

$$\vec{E}_A = -\nabla\phi_e - j\omega\vec{A}, \quad (2.18)$$

where \vec{E}_A is the electric field due to the vector potential \vec{A} . Now that the relationship between \vec{A} and both \vec{E}_A and \vec{H}_A is defined, a vector wave equation for the potential can be derived. By applying a curl operation on both sides of Eqn. (2.15), substituting in Ampere's Law, followed by a substitution of Eqn. (2.18) in for \vec{E}_A , the following equation (assuming a homogeneous medium) is obtained,

$$\nabla^2 \vec{A} + k^2 \vec{A} = -\mu \vec{J} + \nabla(\nabla \cdot \vec{A} + j\omega\mu\epsilon\phi_e) \quad (2.19)$$

Previously, to obtain Eqn. (2.15), only the curl of \vec{A} was defined. To uniquely define a vector, both the curl and the divergence of the vector are required (Helmholtz Theorem). This then implies that the divergence of \vec{A} must be defined. By doing so

Eqn. (2.19), can be simplified. By utilizing the Lorentz Gauge, $\nabla \cdot \vec{A} = -j\omega\mu\epsilon\phi_e$, a simplified vector wave equation for the magnetic vector potential is defined as,

$$\nabla^2 \vec{A} + k^2 \vec{A} = -\mu \vec{J}. \quad (2.20)$$

Additionally, Eqn. (2.18), through the use of the Lorentz Gauge, can be simplified to form,

$$\vec{E}_A = \frac{1}{j\omega\epsilon\mu} [k^2 \vec{A} + \nabla(\nabla \cdot \vec{A})] \quad (2.21)$$

Through a similar type of analysis with electric sources off, but magnetic sources on ($\vec{M} = q_{mv}^i \neq 0, \vec{J} = q_{mv}^i = 0$), the simplified vector wave equation for the electric vector potential can be obtained. The wave equation and the electric and magnetic fields due to the electric vector potential are,

$$\nabla^2 \vec{F} + k^2 \vec{F} = -\epsilon \vec{M}. \quad (2.22)$$

$$\vec{E}_F = -\frac{1}{\epsilon} (\nabla \times \vec{F}) \quad (2.23)$$

$$\vec{H}_F = \frac{1}{j\omega\epsilon\mu} [k^2 \vec{F} + \nabla(\nabla \cdot \vec{F})] \quad (2.24)$$

By comparing Eqn.'s (2.20) and (2.22) to Eqn.'s (2.13) and (2.14), the benefit of the intermediate step of vector potentials is obvious. As for the rest of the process, once the vector potentials have been solved for, the relationship between \vec{A} and both \vec{E} and \vec{H} can be used to obtain the fields due to the potential \vec{A} : \vec{E}_A and \vec{H}_A . Additionally, the relationship between \vec{F} and both \vec{E} and \vec{H} can be used to obtain the fields due to the potential \vec{F} : \vec{E}_F and \vec{H}_F . Finally, the total fields can be obtained by the superposition of the fields due to the potentials, \vec{A} and \vec{F} . This is

summarized below:

$$\vec{E} = \vec{E}_A + \vec{E}_F = \frac{1}{j\omega\epsilon\mu} [k^2 \vec{A} + \nabla(\nabla \cdot \vec{A})] - \frac{1}{\epsilon} (\nabla \times \vec{F}) \quad (2.25)$$

$$\vec{H} = \vec{H}_A + \vec{H}_F = \frac{1}{\mu} (\nabla \times \vec{A}) + \frac{1}{j\omega\epsilon\mu} [k^2 \vec{F} + \nabla(\nabla \cdot \vec{F})] \quad (2.26)$$

To begin the process of determining the total fields, the solution to the vector potential wave equations is needed.

2.4.2.2 Solution to Vector Potential Wave Equations. The solutions to the forced vector wave equations, Eqn.'s (2.20) and (2.22), are given by,²

$$\vec{A}(\vec{r}) = \int_V \mu_0 \vec{J}(\vec{r}') G(\vec{r} | \vec{r}') dV' \quad (2.27)$$

$$\vec{F}(\vec{r}) = \int_V \epsilon_0 \vec{M}(\vec{r}') G(\vec{r} | \vec{r}') dV', \quad (2.28)$$

where $G(\vec{r} | \vec{r}')$ is the free-space Green's function

$$G(\vec{r} | \vec{r}') = \frac{e^{-jk|\vec{r}-\vec{r}'|}}{4\pi|\vec{r}-\vec{r}'|} \quad (2.29)$$

The position vectors, \vec{r} and \vec{r}' , are the observation point and source point, respectively. According to the Green's function, there is a source point singularity at $\vec{r} = \vec{r}'$, which makes determining \vec{J} or \vec{M} extremely difficult. However, when the ultimate goal is to obtain the far-zone scattered fields, the source-point singularity is not an issue when determining the far-field signature. On the other hand, when solving for the currents that produce far-zone scattered fields, it is necessary to solve the integral equations, which require evaluation of fields on the surface or within the volume of the scatterer where $\vec{r} = \vec{r}'$ is possible. Thus, great care must be taken to handle the $\vec{r} = \vec{r}'$ source point singularity.

²For a more in-depth discussion on the forced wave equation solution, reference [1, 7].

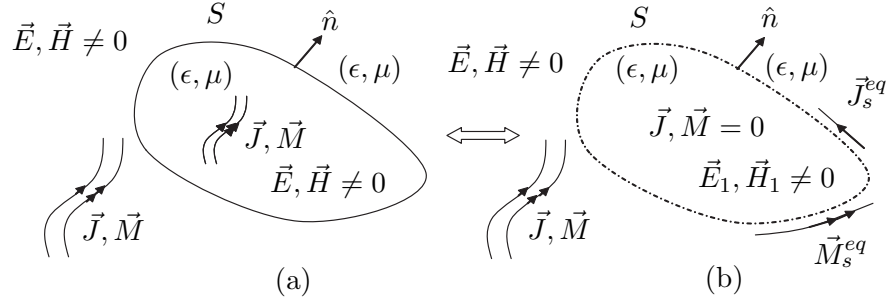


Figure 2.4: (a) Original Problem (b) General Equivalent Problem using surface equivalence principle

To utilize the equations developed in this section (due to the free-space Green's function) the fields of interest must be maintained by equivalent sources $\vec{J}^{eq}/\vec{M}^{eq}$ immersed in unbounded free-space (ϵ_0, μ_0) . To obtain such equivalent sources, the surface equivalent principle can be used [1].

2.4.3 Scattering. Before defining the surface equivalence principle a brief overview of scattering is given. The ultimate goal is to determine the scattered fields, since they are required to determine the Radar Cross Section RCS of a target/scatterer. Reconsider the problem in Fig. 2.3. \vec{E}^i and \vec{H}^i are defined as the incident fields or the fields maintained by the impressed sources, \vec{J} and \vec{M} , in the *absence* of the scatterer. \vec{E} and \vec{H} are defined as the total fields maintained by the impressed sources, \vec{J} and \vec{M} , in the *presence* of the scatterer. Based on the linearity of Maxwell's equations, and the use of superposition the scattered fields can be defined as [1],

$$\vec{E}^s = \vec{E} - \vec{E}^i \quad (2.30)$$

$$\vec{H}^s = \vec{H} - \vec{H}^i \quad (2.31)$$

The basic concept of incident and scattered fields are used throughout the surface equivalence theorem and the formulation of the integral equations.

2.4.4 Surface Equivalence Principle. Often times, when analyzing an electromagnetic problem it is much easier to form an equivalent problem that will yield the same result within a region of interest (typically, an imaginary closed surface). The surface equivalence principle allows us to generate an equivalent problem. Figure 2.4 represents an original problem and its equivalent. The surface equivalence theorem is a principle in which actual objects/inhomogeneities are replaced by equivalent sources. The sources are equivalent *within* a region, in that they radiate the same fields as those scattered by objects replaced [1]. To utilize the surface equivalence principle the equivalent sources must satisfy the boundary conditions on the tangential electric and magnetic field components (which only holds on the surface S):

$$\hat{n} \times (\vec{H} - \vec{H}_1) = \vec{J}_s^{eq} \quad (2.32)$$

$$-\hat{n} \times (\vec{E} - \vec{E}_1) = \vec{M}_s^{eq} \quad (2.33)$$

Since the fields of interest are the fields outside the imaginary surface, the fields within the imaginary surface can be assumed anything. Two specific cases of the surface equivalence principle will be examined. Love's Equivalence Theorem, where the fields within are considered zero, and the Physical Equivalence for a Perfect Electric Conductor, PEC.

2.4.4.1 Love's Equivalence Theorem. Love's Equivalence Theorem is a special case of the surface equivalence principle in that the fields and sources within the imaginary surface are considered zero [7]. If the imaginary surface is condensed until it conforms to the scatterer, then by utilizing Love's Equivalence, Eqn.'s (2.32) and (2.33) reduce to,

$$\hat{n} \times \vec{H}(\vec{r}) = \vec{J}_s^{eq}(\vec{r}) \quad \vec{r} \in S \quad (2.34)$$

$$-\hat{n} \times \vec{E}(\vec{r}) = \vec{M}_s^{eq}(\vec{r}) \quad \vec{r} \in S \quad (2.35)$$

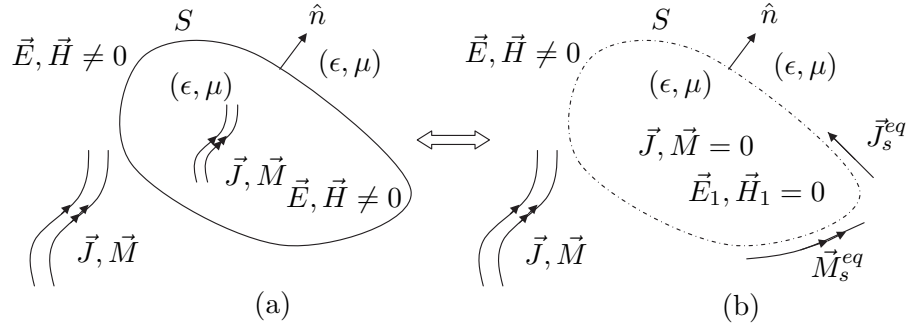


Figure 2.5: (a) Original Problem (b) Equivalent Problem using Love's Equivalence

Figure 2.5 represents the original problem and the equivalent problem using Love's Equivalence Theorem. As previously noted, since the fields in the equivalent problem are maintained by equivalent sources immersed in unbounded free-space, Eqn.'s (2.27) and (2.28) apply with the modification of integrating over the surface, rather than the volume,

$$\vec{A}^s(\vec{r}) = \int_S \mu_0 \vec{J}_s^{eq}(\vec{r}) G(\vec{r} | \vec{r}') dS' \quad (2.36)$$

$$\vec{F}^s(\vec{r}) = \int_S \epsilon_0 \vec{M}_s^{eq}(\vec{r}) G(\vec{r} | \vec{r}') dS' \quad (2.37)$$

Love's equivalence can also be extended to a Perfect Electric Conductor PEC or a Perfect Magnetic Conductor PMC, as long as the scatterer is infinitely planar [1].

2.4.4.2 Physical Equivalence Theorem for a PEC. The Physical Equivalence Theorem for a PEC is another special case of the surface equivalence principle in that the fields within the surface S are assumed to be $-\vec{E}^i$ and $-\vec{H}^i$. According to Fig. 2.6, and utilizing the boundary conditions, Eqn.'s (2.32) and (2.33)

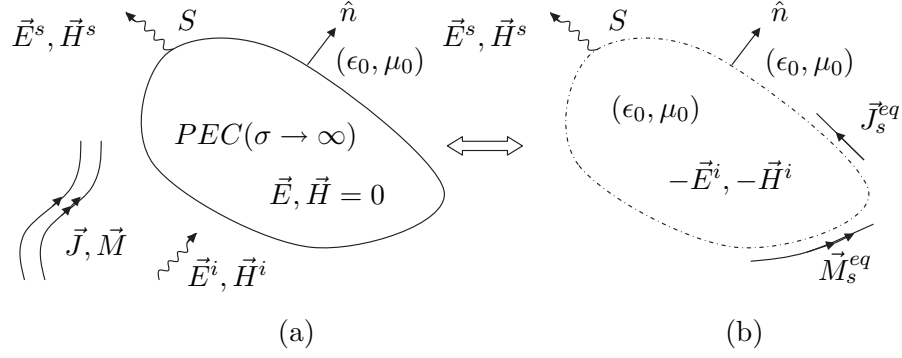


Figure 2.6: (a) Original Problem (b) Equivalent Problem using Physical Equivalence

simplify to,

$$\hat{n} \times (\vec{H} - \vec{H}_1) = \hat{n} \times (\vec{H}^s - (-\vec{H}^i)) = \vec{J}_s^{eq}(\vec{r}) \quad \vec{r} \in S \quad (2.38)$$

$$-\hat{n} \times (\vec{E} - \vec{E}_1) = -\hat{n} \times (\vec{E}^s - (-\vec{E}^i)) = \vec{M}_s^{eq}(\vec{r}) \quad \vec{r} \in S \quad (2.39)$$

Finally, by utilizing Eqn.'s (2.30) and (2.31) and the PEC boundary conditions, Eqn.'s (2.38) and (2.39) reduce to,

$$\hat{n} \times \vec{H}(\vec{r}) = \vec{J}_s^{eq}(\vec{r}) \quad \vec{r} \in S \quad (2.40)$$

$$-\hat{n} \times \vec{E}(\vec{r}) = \vec{M}_s^{eq}(\vec{r}) = 0 \quad \vec{r} \in S \quad (2.41)$$

which are the equivalent currents sources that maintain \vec{E}^s and \vec{H}^s outside S, and $-\vec{E}^i$ and $-\vec{H}^i$ inside S. Since the equivalent sources are immersed in unbounded free-space, Eqn. (2.36) and (2.37) can be used to solve the vector potentials. Finally, with the introduction of the concepts dealing with vector potentials, the solution to the associated vector wave equations, and some basic equivalence principles, the formulation of the integral equations can be accomplished.

2.5 Integral Equation Formulation

Integral equations are often chosen to be the starting point for an electromagnetic scattering analysis. The key to the solution for a scattering problem is to obtain knowledge of the equivalent current densities on the surface of the scatterer. Once these currents are known the scattered fields can be obtained using Eqn.'s (2.36) and (2.37) and Eqn.'s (2.25) and (2.26). Therefore, the goal of the solution method is to accurately predict the currents on the surface of the scatterer [7]. This can be accomplished using integral equations. The following sections will describe how the integral equations are formulated. Each section will be broken up into the electric and magnetic field integral equations, with subsections that deal with specific scattering problems, specifically PEC and Dielectric Scatterers. A brief discussion on the combined field integral equation will follow the formulation of the electric and magnetic field integral equations.

2.5.1 Surface Electric Field Integral Equation. The EFIE is one of the most popular integral equations used in the solution to the scattering problem. The EFIE utilizes the boundary condition on the tangential electric field [1],

$$\hat{n} \times \vec{E}(\vec{r}) = -\vec{M}_s(\vec{r}) \quad \vec{r} \in S \quad (2.42)$$

The following sections will describe the EFIE for a PEC and dielectric scatterer.

2.5.1.1 Perfect Electric Conductor (PEC) Scatterer. The formulation of the EFIE for a PEC scatterer, utilizes the boundary condition that the tangential electric field is zero on a PEC [1],

$$\hat{n} \times \vec{E}(\vec{r}) = 0. \quad \vec{r} \in S \quad (2.43)$$

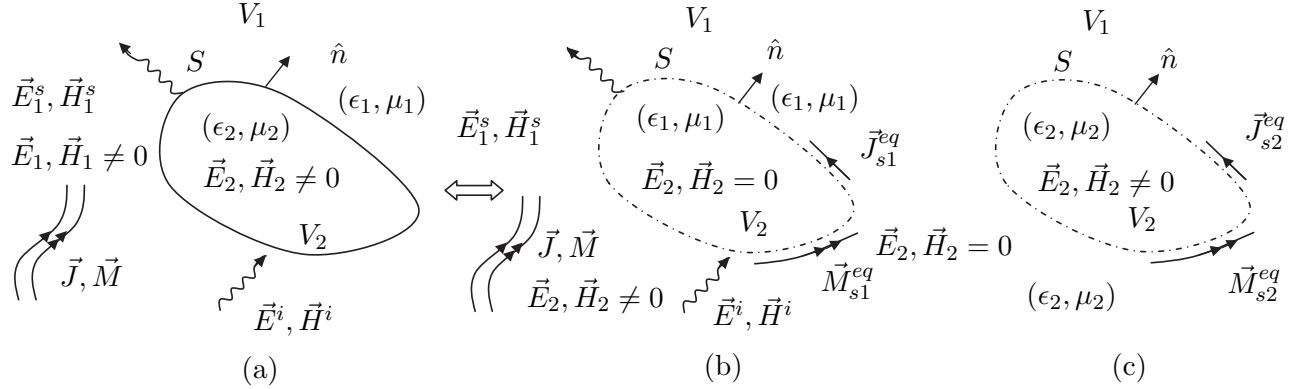


Figure 2.7: (a) Original Problem (b) Exterior Equivalent Problem (c) Interior Equivalent Problem

By substituting Eqn. (2.30) in for $\vec{E}(\vec{r})$, Eqn. (2.43) can be written in the form,

$$\hat{n} \times \vec{E}^s(\vec{r}) = -\hat{n} \times \vec{E}^i(\vec{r}) \quad \vec{r} \in S \quad (2.44)$$

Now utilizing the physical equivalence problem described in Fig. 2.6, and the vector potentials, the EFIE can be written as,

$$\hat{n} \times \frac{1}{j\omega\epsilon_0} (k_0^2 + \nabla \nabla \cdot) \int_S \vec{J}_s(\vec{r}') G(\vec{r} | \vec{r}') dS' = -\hat{n} \times \vec{E}^i(\vec{r}) \quad \vec{r} \in S \quad (2.45)$$

where $\vec{J}_s(\vec{r})$ is the equivalent current as defined in Eqn. (2.40), and \vec{r} is contained on the surface S . According to Eqn. (2.45), the incident electric field, $\vec{E}^i(\vec{r})$, is known, however, $\vec{J}_s(\vec{r})$ is unknown. Once $\vec{J}_s(\vec{r})$ is determined³, the vector potentials can be formed, the corresponding scattered fields can be obtained, and the RCS subsequently computed using Eqn. (2.3).

2.5.1.2 Dielectric Scatterer. When formulating the EFIE for a dielectric scatterer, the original problem must be broken up into an exterior and interior equivalent problem as depicted in Fig. 2.7. The exterior equivalent problem, Fig. 2.7b, invokes Love's equivalence. The equivalent sources $\vec{J}_{s1}^{eq}(\vec{r})$ and $\vec{M}_{s1}^{eq}(\vec{r})$ have

³Refer to Section 2.6

been placed on the surface of the original scatterer and are defined as,

$$\vec{J}_{s1}^{eq}(\vec{r}) = \hat{n} \times \vec{H}_1(\vec{r}) \quad \vec{r} \in S \quad (2.46)$$

$$\vec{M}_{s1}^{eq}(\vec{r}) = -\hat{n} \times \vec{E}_1(\vec{r}) \quad \vec{r} \in S \quad (2.47)$$

where these sources maintain the scattered fields in region one, and in conjunction with the original sources produce the total fields in region one. This is summarized mathematically below,

$$\vec{E}_1(\vec{r}) = \vec{E}^i(\vec{r}) + \vec{E}_1^s(\vec{r}) \quad \vec{r} \in V_1 \quad (2.48)$$

$$\vec{H}_1(\vec{r}) = \vec{H}^i(\vec{r}) + \vec{H}_1^s(\vec{r}) \quad \vec{r} \in V_1 \quad (2.49)$$

According to Fig. 2.7b, since null fields are created within the scatterer, medium two can be replaced with medium one and all theory from Section 2.4.2 can be utilized. The interior equivalent problem is depicted in Fig. 2.7. The equivalent sources $\vec{J}_{s2}^{eq}(\vec{r})$ and $\vec{M}_{s2}^{eq}(\vec{r})$ are defined as

$$\vec{J}_{s2}^{eq}(\vec{r}) = (-\hat{n}) \times \vec{H}_2(\vec{r}) \quad (2.50)$$

$$\vec{M}_{s2}^{eq}(\vec{r}) = -(-\hat{n}) \times \vec{E}_2(\vec{r}) \quad (2.51)$$

where these sources maintain the scattered fields in region two and create null fields throughout region one. This then implies that the scattered fields are the fields within the scatterer,

$$\vec{E}_2(\vec{r}) = \vec{E}_2^s(\vec{r}) \quad \vec{r} \in V_2 \quad (2.52)$$

$$\vec{H}_2(\vec{r}) = \vec{H}_2^s(\vec{r}) \quad \vec{r} \in V_2 \quad (2.53)$$

Again, since the fields in region one are nulled out, medium one can be replaced by medium two, therefore, all theory developed in Section 2.4.2 on vector potentials

can be used. To relate $\vec{J}_{s1}^{eq}(\vec{r})$ to $\vec{J}_{s2}^{eq}(\vec{r})$ and $\vec{M}_{s1}^{eq}(\vec{r})$ to $\vec{M}_{s2}^{eq}(\vec{r})$, the continuity of the tangential electric and magnetic fields at the dielectric interface can be utilized to obtain,

$$\vec{J}_{s1}^{eq}(\vec{r}) = -\vec{J}_{s2}^{eq}(\vec{r}) \quad \vec{r} \in S \quad (2.54)$$

$$\vec{M}_{s1}^{eq}(\vec{r}) = -\vec{M}_{s2}^{eq}(\vec{r}) \quad \vec{r} \in S \quad (2.55)$$

Due to the nature of the problem (2 equivalent problems and 2 unknown sources), a coupled EFIE formulation is needed [7]. Utilizing the theory established in Section 2.4.2 the coupled EFIE can be written as,

$$\hat{n} \times \left[\frac{1}{j\omega\epsilon_1\mu_1} [k_1^2 \vec{A}_1^s + \nabla(\nabla \cdot \vec{A}_1^s)] - \frac{1}{\epsilon_1} (\nabla \times \vec{F}_1^s) \right] + \vec{M}_{s1}^{eq} = -\hat{n} \times \vec{E}^i \quad \vec{r} \in S^+ \quad (2.56)$$

$$\hat{n} \times \left[\frac{1}{j\omega\epsilon_2\mu_2} [k_2^2 \vec{A}_2^s + \nabla(\nabla \cdot \vec{A}_2^s)] - \frac{1}{\epsilon_2} (\nabla \times \vec{F}_2^s) \right] - \vec{M}_{s1}^{eq} = 0 \quad \vec{r} \in S^- \quad (2.57)$$

where the subscripts 1 and 2 denote the medium in which the sources radiate and,

$$\begin{aligned} \vec{A}_1^s(\vec{r}) &= \int_S \mu_1 \vec{J}_{s1}^{eq}(\vec{r}') G_1(\vec{r} | \vec{r}') dS' & \vec{r} \in V_1 \\ \vec{F}_1^s(\vec{r}) &= \int_S \epsilon_1 \vec{M}_{s1}^{eq}(\vec{r}') G_1(\vec{r} | \vec{r}') dS' & \vec{r} \in V_1 \\ \vec{A}_2^s(\vec{r}) &= - \int_S \mu_2 \vec{J}_{s1}^{eq}(\vec{r}') G_2(\vec{r} | \vec{r}') dS' & \vec{r} \in V_2 \\ \vec{F}_2^s(\vec{r}) &= - \int_S \epsilon_2 \vec{M}_{s1}^{eq}(\vec{r}') G_2(\vec{r} | \vec{r}') dS' & \vec{r} \in V_2 \end{aligned}$$

One should note that Eqn. (2.56) is evaluated just outside the surface (S^+), while Eqn. (2.57) is evaluated just inside the surface (S^-). Again, once the equivalent sources are determined, the vector potentials can be obtained, thereby, producing the scattered fields.

2.5.2 Surface Magnetic Field Integral Equation. The MFIE is another popular integral equation used in the solution to the scattering problem. The MFIE utilizes the boundary condition on the tangential magnetic field [1],

$$\hat{n} \times \vec{H} = \vec{J}_s \quad \vec{r} \in S \quad (2.58)$$

The following sections will describe the MFIE for a PEC and dielectric scatterer.

2.5.2.1 Perfect Electric Conductor (PEC) Scatterer. The formulation of the MFIE for a PEC scatterer can be obtained by substituting Eqn. (2.31) for \vec{H} into Eqn. (2.58) and rearranging to form,

$$\hat{n} \times \vec{H}^s - \vec{J}_s = -\hat{n} \times \vec{H}^i \quad \vec{r} \in S \quad (2.59)$$

We are now in a position to invoke the physical equivalence problem described in Fig. (2.6), and the vector potentials, to formulate the MFIE,

$$\hat{n} \times \nabla \times \int_S \vec{J}_s(\vec{r}') G(\vec{r} | \vec{r}') dS' - \vec{J}_s(\vec{r}) = -\hat{n} \times \vec{H}^i \quad \vec{r} \in S \quad (2.60)$$

where \vec{J}_s is the equivalent current as defined in Eqn. (2.40) and \vec{r} is contained just outside the surface S . In the limit as \vec{r} approaches S it can be shown [2] that Eqn (2.60) reduces to Maue's Integral Equation [2],

$$\hat{n} \times \nabla \times \oint_S \vec{J}_s(\vec{r}') G(\vec{r} | \vec{r}') dS' - \frac{1}{2} \vec{J}_s(\vec{r}) = -\hat{n} \times \vec{H}^i \quad \vec{r} \in S \quad (2.61)$$

Again, since the equivalent current is immersed in unbounded free-space the theory from Section 2.4.2 applies.

2.5.2.2 Dielectric Scatterer. To formulate the MFIE for the dielectric scatterer reconsider Fig. 2.7, and the development of Eqn.'s (2.46) through (2.55).

Utilizing the equivalent problems and the boundary condition for the tangential magnetic field, the coupled MFIE for a dielectric is defined as,

$$\hat{n} \times \left[\frac{1}{j\omega\epsilon_1\mu_1} [k_1^2 \vec{F}_1^s + \nabla(\nabla \cdot \vec{F}_1^s)] + \frac{1}{\mu_1} (\nabla \times \vec{A}_1^s) \right] - \vec{J}_{s1}^{eq} = -\hat{n} \times \vec{H}^i \quad \vec{r} \in S^+ \quad (2.62)$$

$$\hat{n} \times \left[\frac{1}{j\omega\epsilon_2\mu_2} [k_2^2 \vec{F}_2^s + \nabla(\nabla \cdot \vec{F}_2^s)] + \frac{1}{\mu_2} (\nabla \times \vec{A}_2^s) \right] + \vec{J}_{s1}^{eq} = 0 \quad \vec{r} \in S^- \quad (2.63)$$

where the subscripts 1 and 2 denote the medium in which the sources radiate and $\vec{A}_1^s(\vec{r})$, $\vec{F}_1^s(\vec{r})$, $\vec{A}_2^s(\vec{r})$, and $\vec{F}_2^s(\vec{r})$ were defined in the EFIE formulation. One should note that Eqn. (2.62) is evaluated just outside the surface S^+ , while Eqn. (2.63) is evaluated just inside the surface S^- . Again, once the equivalent sources are determined, the vector potentials can be obtained, thereby, producing the scattered fields.

2.5.3 Surface Combined Field Integral Equation. When deriving the EFIE or the MFIE either the boundary condition for the tangential electric or magnetic field was enforced. By enforcing the boundary conditions individually, there are scatterers in which the solution is not unique. This is considered the internal resonance problem with the EFIE and the MFIE [8]. The Combined Field Integral Equation, CFIE, is developed to mitigate the internal resonance problem. The CFIE is a linear combination of the EFIE and the MFIE. For a closed conducting surface the CFIE can be defined as,⁴

$$\alpha EFIE + (1 - \alpha) MFIE \quad (2.64)$$

where α is used as a scaling term and as a fix-up to the units. The scaling term ranges from $0 < \alpha < 1$ and typically is set to 0.8. By setting α to zero or one, the CFIE

⁴For complete development reference [9]

reduces to the MFIE or EFIE, respectively. Throughout the development of the EFIE and MFIE, once the integral equation was formulated, if the equivalent sources could be determined then the problem was solved. To solve these equations the use of the Method of Moments can be utilized. The following section will describe how to solve for the equivalent current densities, find the scattered fields, and ultimately determine the RCS of the scatterer.

2.6 Method of Moments (MoM)

MoM is a procedure for solving linear operator equations (such as an integral equation) that have the form:

$$Lf = g \quad (2.65)$$

where in our case L is a linear integral operator on \vec{J} or \vec{M} , g is the known forcing function (typically related to \vec{E}^i), and f being the unknown current density \vec{J} or \vec{M} [10]. By obtaining the induced current density

$$f = L^{-1}g, \quad (2.66)$$

the scattered fields from a target can be obtained from the traditional radiation integrals as defined in Section 2.4.2, Eqn.'s (2.27) and (2.28). To solve Eqn. (2.66) the following procedure must be applied to determine the domain of the operator L . The procedure is [2, 10, 11]:

- Express the unknown function f in terms of a set of basis functions with unknown coefficients

$$f \approx \sum_{n=1}^N a_n e_n \quad (2.67)$$

where a_n is an expansion constant (unknown) and e_n is an expansion function (known)

- Determine a suitable inner product and define weighting functions
- Form the matrix equation by taking the inner product
- Invert the matrix and solve for the unknown coefficients

Typically, the expansion functions that are chosen closely model the physical behavior of the unknown. By doing this, fewer expansion functions are needed, however it may also lead to integrals that cannot be solved in closed form [7]. Additionally, by selecting expansion functions that allow mathematical operations to be performed in closed form allows numerical integration or differentiation to be minimized. As for testing functions they should be chosen such that mathematical operations can be performed in closed form and numerical convergence can be achieved. The expansion and testing functions can be divided into two classes: subdomain and entire domain. Subdomain functions are defined as being non-zero over a portion of the domain, which is typically the scattering surface. Some common subdomain functions are: delta functions, piecewise constant defined as being non-zero over the entire domain of the unknown. Some common entire domain functions are sines, cosines, and polynomials [7]. Recently many MoM codes have been implemented to take advantage of the processing capabilities of today's computers. The following section will describe the three dimensional MoM code, CARLOS [12], that was utilized in providing computational results to the model which will be described in Chapter III.

2.6.1 CARLOS. Code for Analysis of Radiators on Lossy Surfaces, or CARLOS, is a general purpose MoM code that calculates radiation or scattering from complex geometries. As mentioned, CARLOS, is a general MoM code that utilizes the Galerkin Method, which signifies that the testing and basis functions are of the same type, to solve the Stratton-Chu integral equations [13]. The Stratton-Chu integral equations are identical to the EFIE and MFIE developed earlier. For the

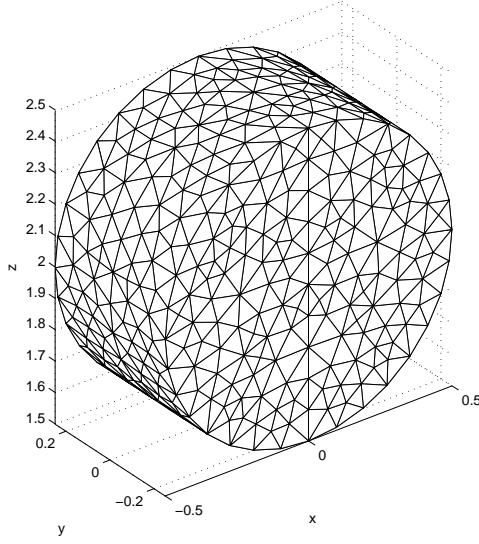


Figure 2.8: Example ACAD generated facet file.

testing and basis functions CARLOS utilizes the RWG basis functions. RWG basis functions are defined over pairs of adjacent triangles with the current approximated by flowing between two opposite vertices, across their common edge. The current component normal to the common edge is continuous and since the current has no component normal to the boundaries of the triangles, there exists no line charges [14]. CARLOS offers many input parameters to accommodate many different types of geometries. CARLOS has the option of analyzing bodies of revolution, two-dimensional bodies of translation, three-dimensional wires, and three-dimensional triangular and quadrilateral patch surfaces. Within the user input file, the geometry must be in a format that CARLOS can read. Throughout this research all geometry facet files were created using Advanced Computer Aided Design, ACAD [15]. An example of an ACAD generated facet file is depicted in Fig. 2.8. The mesh utilized has certain suggested criterion for accurate computations. The criteria are [12]:

- Grid Density such that maximum edge length is less than $\frac{\lambda}{10}$
- Increased Mesh Densities Near Edges, and Surface and Material Discontinuities

- Maximize Aspect Ratio (i.e. Equilateral Triangles best case scenario)
- Matching Nodes at different surfaces

For a complete theoretical background on the CARLOS code, please refer to [12].

III. Methodology

In this chapter we define the methodology used to isolate and characterize the interaction between the target and mount in Radar Cross Section (RCS) measurements. The methodology presented explains how to isolate and characterize the interaction. Two approaches were applied to validate the isolation and characterization of the interaction. The first approach computationally isolated the interaction of two simple geometry objects utilizing the three-dimensional Method of Moments (MoM) code CARLOS and validated against measurements taken in AFIT's RCS range. The second approach modeled a general target-mount calibration configuration in a RCS range. The mount model replicated the forward canted ogive cross-section pylon, and the target was modeled as a calibration target. This research is carried out through simulations in CARLOS due to the complexity of the system being analyzed. The primary goal of the research is to obtain a modified vector background subtraction equation to account for the interaction between the calibration target and mount. The modified equation, Eqn. (1.3), that includes the interaction term is:

$$\sigma_{tgt} = \frac{|\vec{E}_{tgt}^s - \vec{E}_{bkg}^s|^2}{|\vec{E}_{cal}^s - \vec{E}_{cbk}^s - \vec{E}_{cint}^s|^2} \sigma_{cal} \quad (3.1)$$

3.1 Generalized Isolation Process of the Interaction Scattering Mechanism

The interaction between the target and the mount must first be isolated prior to the characterization. The concept of isolation is quite simple. Recall that the RCS (σ) of a target is defined as [2],

$$\sigma = \lim_{R \rightarrow \infty} 4\pi R^2 \frac{|\vec{E}^s|^2}{|\vec{E}^i|^2}, \quad (3.2)$$

where \vec{E}^s is a spherical wavefront, but “locally” planar at $R \rightarrow \infty$, and \vec{E}^i is the planar wavefront incident upon the target. Typically, the incident field is assumed to have a magnitude of one, therefore, the scattered electric field is related to the RCS by,

$$\lim_{R \rightarrow \infty} |\vec{E}| \propto \sqrt{\sigma} \quad (3.3)$$

If the RCS is known, the scattered electric field magnitude can be determined. However, in most radar systems, the in-phase and quadrature (I and Q) data is measured and available to the operator. In-phase and quadrature data is analogous to the real and imaginary components of a complex number. Therefore, the I and Q data preserves the phase information and fields can be coherently added or subtracted [6]. From a computational standpoint, the three-dimensional Method of Moments (MoM) code, CARLOS, is used specifically to obtain the interaction term in the ogive cross section pylon and target configuration. CARLOS provides two outputs: 1) a field file with complex scattered fields stored in a format conducive to coherent addition/subtraction, and 2) the complex surface current densities at facet centroids which can then be radiated to the far-field utilizing the radiation integrals developed in Sec. 2.4.2.2 to obtain the far-zone scattered fields [12].

The concept of coherence is the key element in isolating the interaction. The interaction isolation process is similar to the vector background subtraction technique introduced in Sec. 2.3. The interaction isolation process requires, through measurements or CARLOS simulations, the following scattered fields:

\vec{E}_{tm}^s : The scattered field due to the target-mount configuration. Contained within this field is the interaction, \vec{E}_{int}^s , between the target and mount.

\vec{E}_t^s : The scattered field due to the target “floating” in free-space. Although this measurement may not be physically realizable, simulated results are used to

characterize the interaction between the calibration target-mount configuration.

\vec{E}_m^s : The scattered field due to the mount. In the simple cylinder geometry case, the \vec{E}_m^s measurement can be taken. However, in the ogive mount-target configuration, the \vec{E}_m^s measurement *cannot* be physically taken. This is due to the ogive's top termination, which is “invisible” to the radar when measuring \vec{E}_{tm}^s , but visible when measuring \vec{E}_m^s . Section 3.3.1 describes the computational process to obtain the scattered field due to the mount in the calibration target-mount configuration.

The general technique to isolate the interaction is summarized in Fig. 3.1 and mathematically represented by

$$\vec{E}_{int}^s = \vec{E}_{tm}^s - (\vec{E}_t^s + \vec{E}_m^s) \quad (3.4)$$

Isolating the interaction scattering mechanism requires *coherently* subtracting the sum of the scattered fields due to the target (\vec{E}_t^s) and mount (\vec{E}_m^s) from the total scattered electric field from the target-mount configuration (\vec{E}_{tm}^s). The following sections describe the experimental setup used to obtain the RCS measurements of the target, mount, and calibration target-mount configurations required for interaction isolation. The first section provides a simple two cylinder geometry as a proof of concept in which physical measurements are validated against computational results. The second section describes the RCS measurement setup used to characterize the interaction between the calibration target and ogive cross section pylon.

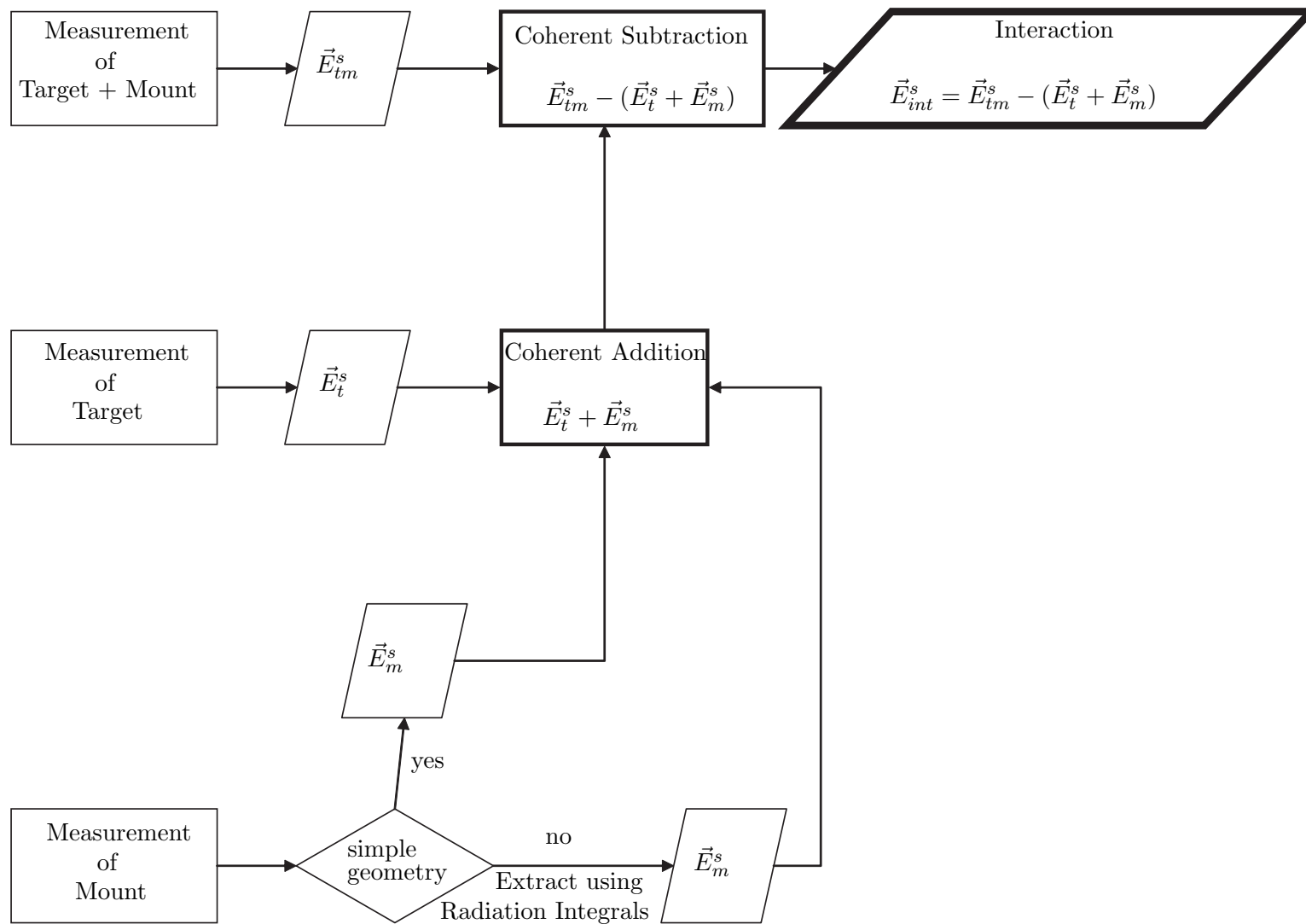


Figure 3.1: Summary of methodology of isolating the interaction scattering mechanism. Chart is read from left to right. Square boxes represent processes that must be carried out, trapezoids represent data from the processes, and the diamond represents a decision that must be made by the user.

3.2 Proof of Concept: A Simple Two Cylinder Geometry

This section specifies the geometry and parameters applied to isolate and characterize the interaction between two, right circular cylinders. The geometry was selected since the configuration inherently contains a significant contribution from electromagnetic coupling (i.e. interaction) between the two cylinders. In fact, the electrical separation distance varies with increasing frequency and demonstrates the effects of frequency on the interaction between multiple scatterers. The simple configuration allows measurements in the AFIT RCS range. The comparison between measured and computational results validate the isolation process. The Perfect Electric Conductors (PEC), cylinders 1 and 2 in Fig. 3.2, separately represent the RCS measurement mount and target, respectively. The combination represents the target-mount configuration for a RCS measurement. The following sections describe the analytical tools used to characterize the interaction. The analyses include three independent methods: three-dimensional Method of Moments (MoM) computations (CARLOS), physical measurements, and the high frequency computations (GO).

3.2.1 Computational Experimental Setup. Computationally, the problem is set up utilizing CARLOS. The simulation geometry must be specified to begin obtain the RCS from CARLOS. To accomplish this task, the geometry is meshed as triangular or quadrilateral patches. As stated in Sec. 2.6.1, CARLOS utilizes RWG basis functions. Therefore, the geometry in Fig. 3.2 is triangularly meshed using ACAD. The resultant simple cylinder mesh is depicted in Fig. 3.3. The mesh properties meet the generally accepted guidelines summarized in Sec. 2.6.1. Using the conventional spherical coordinate system (θ measured from the $+\hat{z}$ -axis and ϕ measured from the $+\hat{x}$ -axis), a monostatic frequency sweep measurement is performed. A monostatic frequency sweep measurement is an RCS measurement in which the frequency is varied, while the target is fixed at some θ and ϕ . Since the objective of this research is to characterize the interaction in calibration measurements, the model is oriented to replicate a standard calibration setup in physical measurements. A monostatic

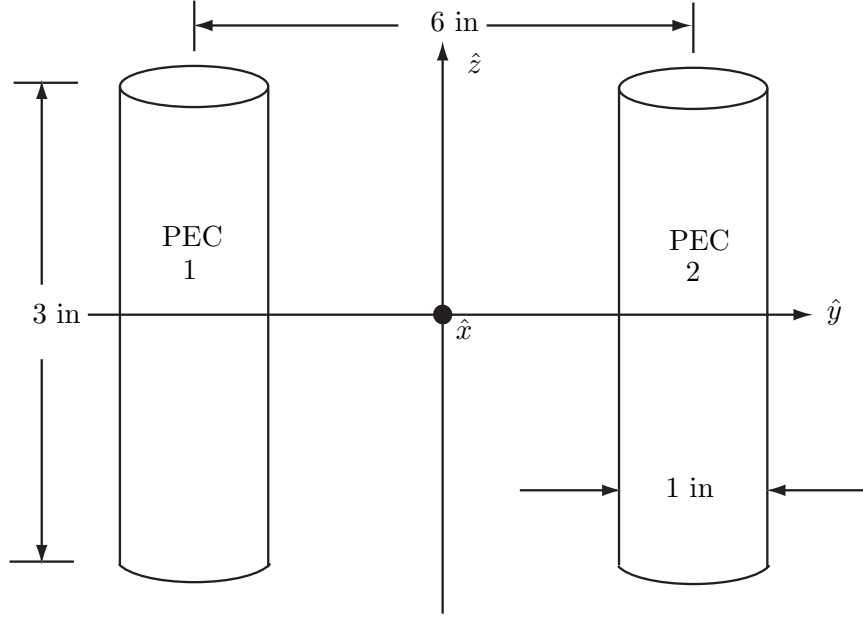


Figure 3.2: Geometry utilized to isolate the interaction term. Perfect Electric Conducting (PEC) Cylinder 1 represents the mount, PEC Cylinder 2 represents the target, and the combination of both cylinders represent the target-mount configuration in a RCS measurement

frequency sweep is taken over a frequency span of 6.2 GHz to 10.2 GHz by 200 MHz increments, with $\theta = 90^\circ$, and $\phi = 0^\circ$. The setup accommodates a frequency band within the operating limits of the AFIT range radar, and the angular orientation is representative of a standard calibration setup. Both horizontal and vertical polarizations are explored to determine the polarization dependence of the interaction. In total six simulations are carried out to isolate the interaction scattering mechanism between the cylinders in each polarization. The interaction is isolated through the process defined in Sec. 3.1. That is, the interaction between the two cylinders is isolated by coherently subtracting the *computed* far-zone scattered fields in each configuration. The configurations are: cylinder 1 alone which scatters \vec{E}_m^s , cylinder 2 alone which scatters \vec{E}_t^s , and finally the combination of both cylinders which scatters \vec{E}_{tm}^s . The results and analysis are presented in Chapter IV.

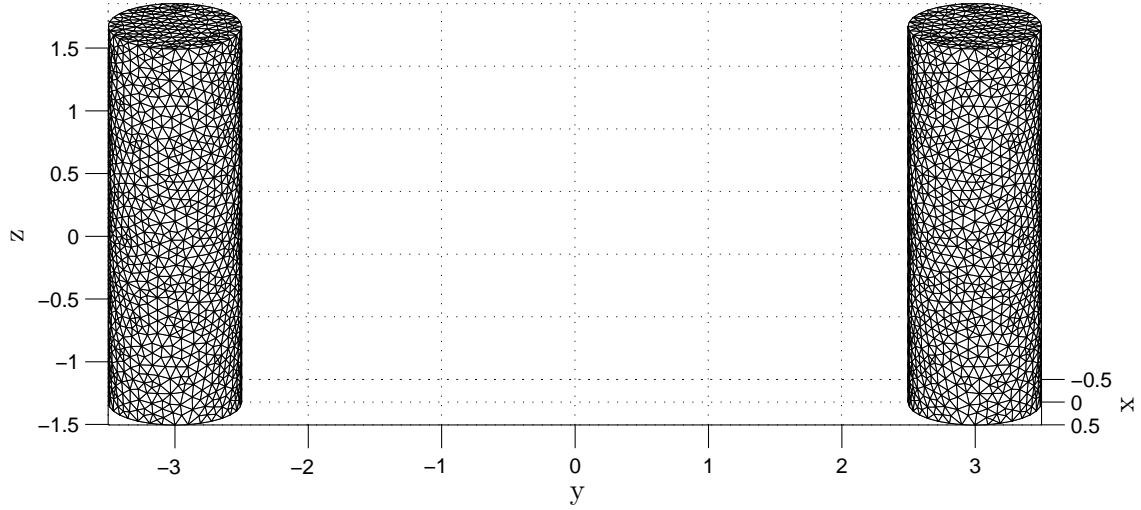


Figure 3.3: Triangular Mesh used as input to CARLOS for the cylinder geometry. Mesh meets all requirements as specified in Section 2.6.1

3.2.2 RCS Measurement Setup. The computational results are compared to measurements taken in the AFIT RCS range. The experimental setup is shown in Fig. 3.4. The experimental setup consists of two 3-inch length by 1-inch diameter aluminum cylinders separated by 6 inches center-to-center. Individually the two cylinders represent the mount and target in a RCS measurement. A monostatic frequency sweep is taken over a frequency span of 6.2 GHz to 10.2 GHz by 200 MHz increments with $\theta = 90^\circ$ and $\phi = 0^\circ$. Both horizontal and vertical polarizations are exploited to determine the polarization dependence of the interaction.

The interaction between the two cylinders is isolated by coherently subtracting the *measured* far-zone scattered fields in each configuration. The configurations are: cylinder 1 alone which scatters \vec{E}_m^s , cylinder 2 alone which scatters \vec{E}_t^s , and finally the combination of both cylinders which scatters \vec{E}_{tm}^s . The results and analysis of the physical measurements are presented in Chapter IV.

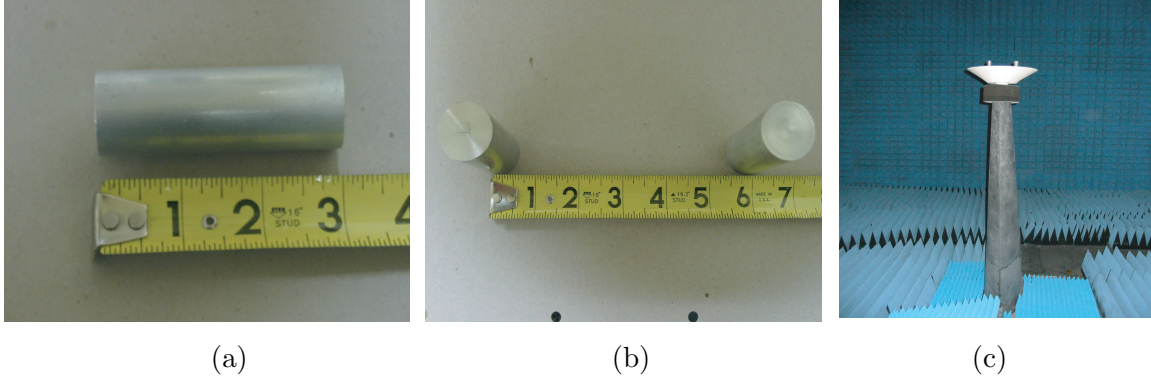


Figure 3.4: Pictures of experimental setup. (a) Physical dimensions of the cylinders utilized. (b) Separation distance between the two cylinders. (c) Measurement configuration in the range as seen by the radar.

The primary goal of these measurements is to validate the isolation process. However, neither the computational results nor the physical measurements provide sufficient physical insight into what is occurring in the configuration, therefore, a Geometrical Optics (GO) analysis is included. The following section provides the basis for the GO analysis that is carried out in Chapter IV.

3.2.3 Geometric Optics Setup and Approximation. Geometric Optics is a high frequency ray tracing technique to obtain the scattered field. Geometric Optics obeys Snell’s Law of Reflection, in that the incident angle is equal to the reflected angle [1]. An important GO analysis characteristic is the returns can be isolated and coherently summed to obtain a particular configuration’s total scattered field. The GO analysis on the simple two-cylinder geometry allows us to isolate the specular returns (denoted i), and the “double bounce” (denoted ii) returns illustrated in Fig. 3.5. The specular return, measured on a single cylinder is either \vec{E}_t^s or \vec{E}_m^s in the isolation process. The specular return is the dominant return in the GO analysis. The “double bounce” return is $2\vec{E}_{int}^s$, and can be envisioned as the incident ray upon the cylinder at Q_1 , reflected to the second cylinder at Q_2 , and finally reflected back to the radar. In the two-cylinder configuration, the dominant returns are the two specular returns (one from each cylinder) and two “double bounce” returns, which

result in \vec{E}_{tm}^s in the isolation process. Appendix A provides the analysis to obtain the far zone scattered fields for each polarization presented here by

Vertical Polarization (VV-Pol):

$$\vec{E}^i = \hat{z}E_0e^{-jk_0x} \quad (3.5)$$

$$\vec{E}_{t,m}^s = -\hat{z}E_0e^{j2k_0a}\sqrt{\frac{a}{2}}\frac{e^{-jk_0R}}{\sqrt{R}} \quad (3.6)$$

$$\vec{E}_{int}^s = \hat{z}E_0e^{jk_0(2a\sin\theta_i-\ell)}\frac{a\cos\theta_i}{2\sqrt{a\cos\theta_i+\ell}}\frac{e^{-jk_0R}}{\sqrt{R}} \quad (3.7)$$

$$\vec{E}_{tm}^s = 2\vec{E}_{t,m}^s + 2\vec{E}_{int}^s \quad (3.8)$$

Horizontal Polarization (HH-Pol):

$$\vec{E}^i = -\hat{y}E_0e^{-jk_0x} \quad (3.9)$$

$$\vec{E}_{t,m}^s = \hat{y}E_0e^{j2k_0a}\sqrt{\frac{a}{2}}\frac{e^{-jk_0R}}{\sqrt{R}} \quad (3.10)$$

$$\vec{E}_{int}^s = \hat{y}E_0e^{jk_0(2a\sin\theta_i-\ell)}\frac{a\cos\theta_i}{2\sqrt{a\cos\theta_i+\ell}}\frac{e^{-jk_0R}}{\sqrt{R}} \quad (3.11)$$

$$\vec{E}_{tm}^s = 2\vec{E}_{t,m}^s + 2\vec{E}_{int}^s \quad (3.12)$$

where a is the cylinder radius, $\ell = d - 2a\cos\theta_i$, and $\theta_i = \frac{\pi}{4}$.

Applying the two-dimensional definition of RCS, in conjunction with Equations (3.6) through (3.12), and then applying the two-dimensional to three-dimensional transformation (derived in Appendix A), the RCS of each return is:

$$\sigma_{go(t,m)} = ka\ell_c^2 \text{ (VV-and-HH-Pol)} \quad (3.13)$$

$$\sigma_{go(int)} = \frac{k(a\cos\theta_i\ell_c)^2}{a\cos\theta_i+\ell} \text{ (VV-and-HH-Pol)} \quad (3.14)$$

$$\sigma_{gotm} = 8k\ell_c^2 \left| e^{jk_0(2a\sin\theta_i-\ell)} \frac{a\cos\theta_i}{2\sqrt{(a\cos\theta_i+\ell)}} \pm e^{j2k_0a} \sqrt{\frac{a}{2}} \right|^2 \quad (3.15)$$

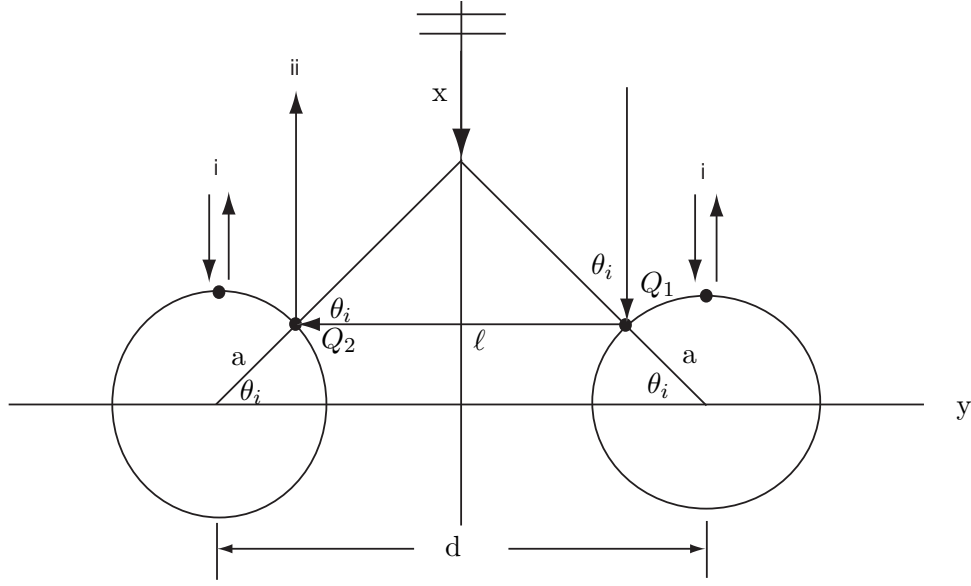


Figure 3.5: Two-dimensional view of the simple cylinder geometry. Geometry was utilized for the GO analysis. The only returns considered were the direct specular scattering and the “double-bounce” scattering mechanism.

where ℓ_c is the length of the cylinders, σ_{go} is the RCS of a single cylinder, σ_{goint} is the RCS of the interaction term, and σ_{gotm} is the RCS of the combination of cylinder 1 and 2. In horizontal polarization (HH-pol), the fields that produce σ_{gotm} sum coherently (+ in Eqn. (3.15)), while the fields subtract coherently (- in Eqn. (3.15)) in vertical polarization (VV-pol). Figure 3.5 illustrates the two specular and two “double-bounce” returns. The effects of diffraction, creeping wave returns, and higher order bounces are neglected in the GO analysis. The results are presented in Chapter IV.

3.3 Pylon Model and Its Parameters

Once the process of isolating the interaction scattering mechanism is validated against the simple cylinder geometry, a more complex target-mount configuration is modeled to characterize the interaction. Due to the complexity of the configurations, the target-mount configuration will be carried out computationally. Figure 3.6

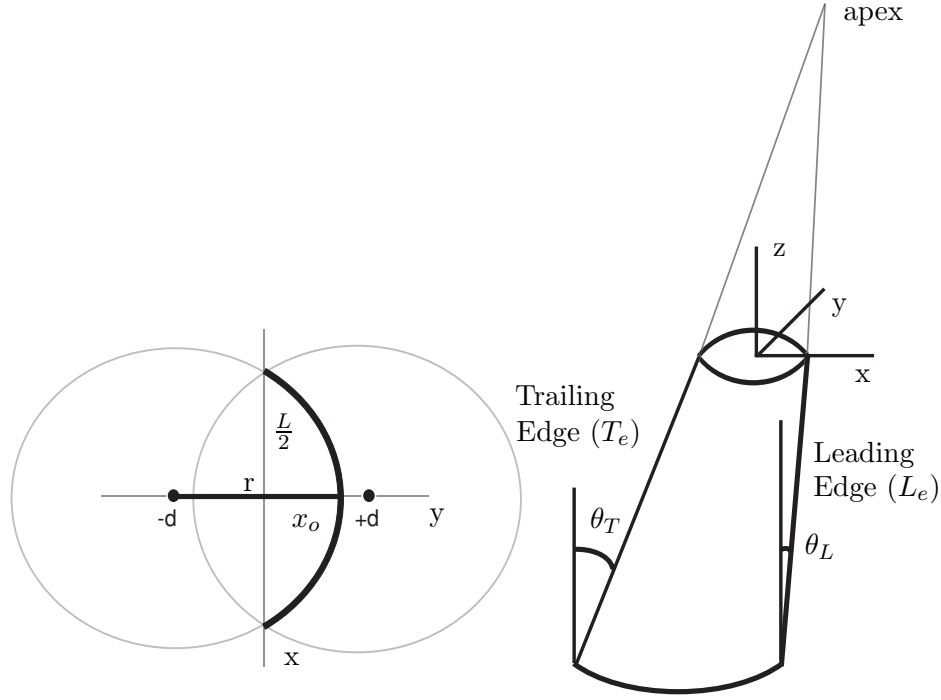


Figure 3.6: Geometry of an ogive cross section pylon. The radius of curvature, r , defines the circle centered at $(0, \pm d)$. $\frac{L}{2}$ and x_o describe the semi-major and semi-minor axis lengths of the ogive, respectively. θ_L and θ_T represent the angles off normal from the leading and trailing edges, respectively.

illustrates the pylon geometry. The ogive cross-section pylon is defined as the cross-section with the radius of curvature of a circle centered at $(0, \pm d)$, and half major and minor axes of lengths $L/2$ and x_o , respectively. Through geometrical analysis the radius r and distance d can be obtained if the ogive parameters L and x_o are specified. The radius of the circle r and distance from the origin d are mathematically represented by

$$r = \frac{4x_o^2 + L^2}{8x_o} \quad (3.16)$$

$$d = r - x_o \quad (3.17)$$

The ogive's geometrical description would be incomplete without defining the leading and trailing edge lengths (L_e and T_e) and their corresponding angles. The leading

Table 3.1: Ogive Pylon Parameters

Top		Bottom
L	7 inch	21 inch
x_o	1 inch	3 inch
Vertical Dimensions		
θ_T	46.5°	
θ_L	25°	
T_e	28.32 inch	
L_e	21.25 inch	

edge is specified by a off-normal angle (θ_L), and the trailing edge by an off-normal angle (θ_T). The leading and trailing edges meet at an apex which is depicted in Fig. 3.6. The pylon parameters are listed in Table 3.1. It is unrealistic to model an infinite length pylon so only a portion is modeled. Modeling a portion of the pylon is a suitable technique since physical measurement techniques try to minimize the unwanted returns, but certain issues arise and need to be considered. In physical RCS measurements there are techniques that mitigate the returns from the lower portion of the ogive pylon. In particular, hardware range gating, as described in Sec. 2.3.1.1, helps mitigate the returns from the traveling wave down the knife edge of the ogive pylon. From a computational standpoint, hardware range gating cannot be accomplished, therefore, it may be necessary to utilize other techniques to suppress the returns from the traveling wave down the ogive. The traveling wave caused by the sharp discontinuity (termination) at the base of the pylon creates a standing wave on the pylon surface due to the forward and reverse traveling waves. Thus, impedance surface treatments may be needed to mitigate the returns from the “shorter” pylon and the termination to accurately simulate the RCS measurement. The termination effects are assessed in Chapter IV. Another effect is the field taper in RCS measurements. Outside the quiet zone where the wavefront is no longer considered planar, the field has both an amplitude and phase taper. In measurements, these returns can be mitigated through the use of range gating. However, within

simulations there is no way to range gate nor to specify a quiet zone. Moreover, the incident field cannot be decomposed into planar wavefronts for one region and spherical wavefronts outside that region. Since the spherical wavefront contributions in physical measurements are assumed to be negligible, we assume minimal contributions in simulations as well. The ogive model just described, in conjunction with two calibration targets, are used to characterize the interaction.

3.3.1 Computational Setup for the Pylon-Cylinder Model. To isolate and characterize the interaction between the calibration target and mount, the mount described in Sec. 3.3 is *simulated* computationally with two calibration objects placed in the target-mount configuration, as shown in Fig. 3.7. The two calibration targets are: 1) a 15-inch diameter x 3.5-inch height cylinder (denoted “1500x350”) and 2) a 18-inch diameter x 12-inch height cylinder (“denoted 1800x1200”). The cylinders were chosen to be representative of calibration targets, and to explore the functional dependence of the interaction on target geometry. The simulations parallel those performed for the simple two-cylinder geometry. The only difference is the frequency range over which the measurements are taken. The complexity of the configuration and the computational size of the problem dictate this change. Each triangular facet edge represents an unknown that must be solved. Also a denser grid is suggested to satisfy a minimum edge length of $\lambda/10$ for moderate accuracy within CARLOS at higher frequencies. For example, doubling the frequency reduces the minimum facet edge length by one half. This quadruples the number of edges which directly relates to an increase of 64 times the amount of computational time. Therefore, lower frequencies were specified to minimize computer processing time. The simulations on the 1800x1200 and 1500x350 calibration target-mount configuration consisted of a monostatic frequency sweep of 100 MHz to 4.033 GHz by 192 MHz and 96 MHz increments, respectively, with angular orientations of $\theta = 90^\circ$ and $\phi = 0^\circ$ in vertical and horizontal polarizations.

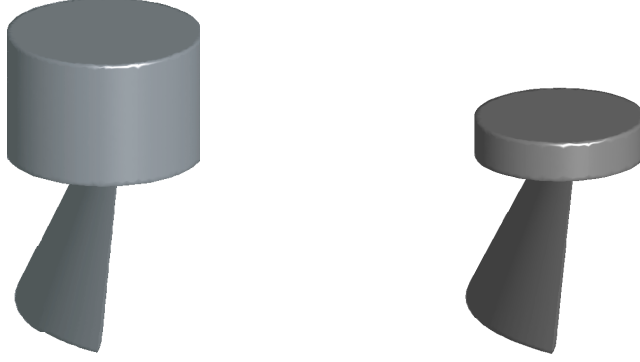


Figure 3.7: Representation of the target-mount configurations utilized computationally for the isolation and characterization of the interaction. The configuration on the left represents an 1800x1200 (18 inch x 12 inch) calibration target, whereas the configuration on the right represents a 1500x350 (15 in diameter x 3.5 in height) calibration target.

3.3.2 Isolation of the Interaction in the Calibration Target-Mount Configuration. The shadowing of the top of the pylon by the target in the target-mount configuration does not allow the general isolation process developed in Sec. 3.1 to be applied directly. The direct measurement of the scattered fields due to the mount *cannot* be carried out due to the termination at the top of the ogive present in the measurement obtaining \vec{E}_m^s , but “invisible” to the radar in the measurement obtaining \vec{E}_{tm}^s . Therefore, an extraction of the mount’s far-field signature in the *presence* of the calibration target must be performed. CARLOS provides the complex surface current densities $\vec{J}^s(\vec{r}')$ at facet centers. The radiation integrals developed in Sec. 2.4.2.2 are utilized to obtain the far-zone scattered fields due to the mount. It is more convenient to utilize the \vec{N} and \vec{L} vectors (where $\vec{L} = 0$ since there are no magnetic currents) developed by [1] to obtain the far-zone scattered fields. Therefore, Equations (3.18) and (3.19) are used to extract the scattered electric field due

to the mount. The \vec{N} vectors are defined as,

$$N_\theta(\theta, \phi) = \int_S [J_x(\vec{r}') \cos \theta \cos \phi + J_y(\vec{r}') \cos \theta \sin \phi - J_z(\vec{r}') \sin \theta] e^{jkr' \cos \psi} ds' \quad (3.18)$$

$$N_\phi(\theta, \phi) = \int_S [-J_x(\vec{r}') \sin \phi + J_y(\vec{r}') \cos \phi] e^{jkr' \cos \psi} ds' \quad (3.19)$$

where J_x , J_y , and J_z are the x-, y-, and z-components of the electric current density on the surface, S s of the target and mount, \vec{r}' is the position vector from the origin to a source point on S , \vec{r} is the position vector from the origin to an observation point, and ψ is the angle between $\vec{r}(\theta, \phi)$ and \vec{r}' . Once N_θ and N_ϕ are obtained, E_θ and E_ϕ are found via

$$E_\theta(r, \theta, \phi) \simeq -\frac{jk e^{-jkr}}{4\pi r} [\eta_0 N_\theta(\theta, \phi)] \quad (3.20)$$

$$E_\phi(r, \theta, \phi) \simeq -\frac{jk e^{-jkr}}{4\pi r} [\eta_0 N_\phi(\theta, \phi)] \quad (3.21)$$

where E_θ and E_ϕ are the θ and ϕ components of the radiated electric field, r is the distance from the origin to the observer (radar), and η_0 is the impedance of free-space, $120\pi \Omega$. In the calibration configuration, $\hat{r} = -\hat{x}$, $\theta = \pi/2$, $\phi = 0$, $r' \cos \psi = x'$, and $r = -x$, therefore, equations (3.18) and (3.19) reduce to

$$N_\theta\left(\frac{\pi}{2}, 0\right) = -\sum_n \int_{S_n} J_z(\vec{r}') e^{jkx'} ds' \quad (3.22)$$

$$N_\phi\left(\frac{\pi}{2}, 0\right) = \sum_n \int_{S_n} J_y(\vec{r}') e^{jkx'} ds' \quad (3.23)$$

where J_z and J_y were previously defined for Equations (3.18) and (3.19). The following assumptions allow us to evaluate Equations (3.22) and (3.23) in closed form:

- The triangular facets are electrically small, therefore, the current density on each is approximately constant

- The fields radiated by the current density on a facet are nearly identical to those radiated by a Hertzian dipole located at the facet centroid
- The current on the Hertzian Dipole is given by:

$$N_\theta\left(\frac{\pi}{2}, 0\right) = - \int_S J_z(\vec{r}') e^{jkx'} ds' \simeq -J_z(\vec{r}') e^{jkx'} A \quad (3.24)$$

$$N_\phi\left(\frac{\pi}{2}, 0\right) = \int_S J_y(\vec{r}') e^{jkx'} ds' \simeq J_y(\vec{r}') e^{jkx'} A \quad (3.25)$$

where A is the area of the facet

Applying the assumptions, Equations (3.22) and (3.23) reduce to,

$$N_\theta = - \sum_n J_z(\vec{r}'_n) A_n e^{jkx'} \quad (3.26)$$

$$N_\phi = \sum_n J_y(\vec{r}'_n) A_n e^{jkx'} \quad (3.27)$$

where n represents the n^{th} facet. Once N_θ and N_ϕ are obtained, Equations (3.20) and (3.21) are employed to calculate E_θ and E_ϕ , which ultimately yield the far-zone scattered fields due to the currents on an arbitrary surface. It should be noted that in this configuration, E_θ corresponds to vertical polarization, and E_ϕ corresponds to horizontal polarization. The assumptions made to extract the far-zone scattered fields will be validated against CARLOS' results in Chapter IV.

Now that the tool for extracting the far-zone scattered fields due to the currents on an arbitrary surface is built, the scattered fields caused by the mount are obtainable. From that point forward, the isolation process developed in Sec. 3.1 is used. Simulations of the 1500x350 and 1800x1200 calibration targets in free space are performed to obtain the scattered field due to the target, \vec{E}_t^s . Finally, the scattered field due to the calibration target-mount configuration is simulated to obtain \vec{E}_{tm}^s . Utilizing the scattered fields obtained through the simulations in conjunction with

Eqn. (3.4) the interaction can be isolated and characterized in a general manner. Results obtained utilizing the modified extraction method and the isolation process are presented in Chapter IV.

3.4 “Difference” Currents

This section utilizes the extraction method developed in the previous section to look at the difference currents on the surface of the calibration target in the presence and absence of the pylon. This process is identical to coherently subtracting the effects of the mount in the far-field, but the subtraction is carried out in the near-field and then radiated to the far-field. The purpose of this section is to look at the perturbations on the target in the presence and absence of the mount to obtain an understanding of the pylon effects on the target. The ultimate goal of looking at the difference currents on the surface of the target is to gain physical insight into the interaction. All results are presented in Chapter IV.

IV. Results and Analysis

This chapter contains the results and analysis for the two experimental/computational setups described in Chapter III. Results for the simple cylinder geometry are presented first followed by results for the two calibration target-mount configurations. Recall that the simple two cylinder case was developed as a proof of concept for isolating the interaction scattering mechanism. Results for the calibration target-mount configuration are used to characterize the interaction for both calibration targets simulated in CARLOS.

4.1 Two Cylinder Geometry

The simple two-cylinder geometry serves to validate the isolation process described in Sec. 3.1. Consider again the geometry in Fig. 3.2. The experimental setup consisted of two, 3-inch long x 1-inch diameter right circular cylinders separated by a center-to-center distance of 6 inches. The measurements consisted of monostatic frequency sweeps from 6.2 GHz to 10.2 GHz in 200 MHz increments, at an aspect of $\theta = 90^\circ$ and $\phi = 0^\circ$, in which both horizontal and vertical polarizations were exploited. The measurements taken, both computationally and in a RCS range, are utilized in conjunction with Eqn. (3.4) to isolate the interaction.

4.1.1 Perfect Electric Conductor (PEC) Cylinder 1 and 2 Results. PEC cylinders 1 and 2 represent the mount and target in a RCS measurement. Therefore, the far-zone scattered fields due to each individual cylinder are denoted as in the isolation process \vec{E}_m^s and \vec{E}_t^s , respectively. Moment Method, RCS measurements, and Geometric Optics (GO) results are shown in Fig. 4.1 for cylinder 1 and 2. The plots indicate the RCS for cylinder 1 and 2 in each polarization are virtually identical when measured individually. Small variations in the RCS levels for different polarizations are attributable to the scattering mechanisms inherent in the particular polarization. In both polarizations, the dominant scattering mechanism is specularly off the singly

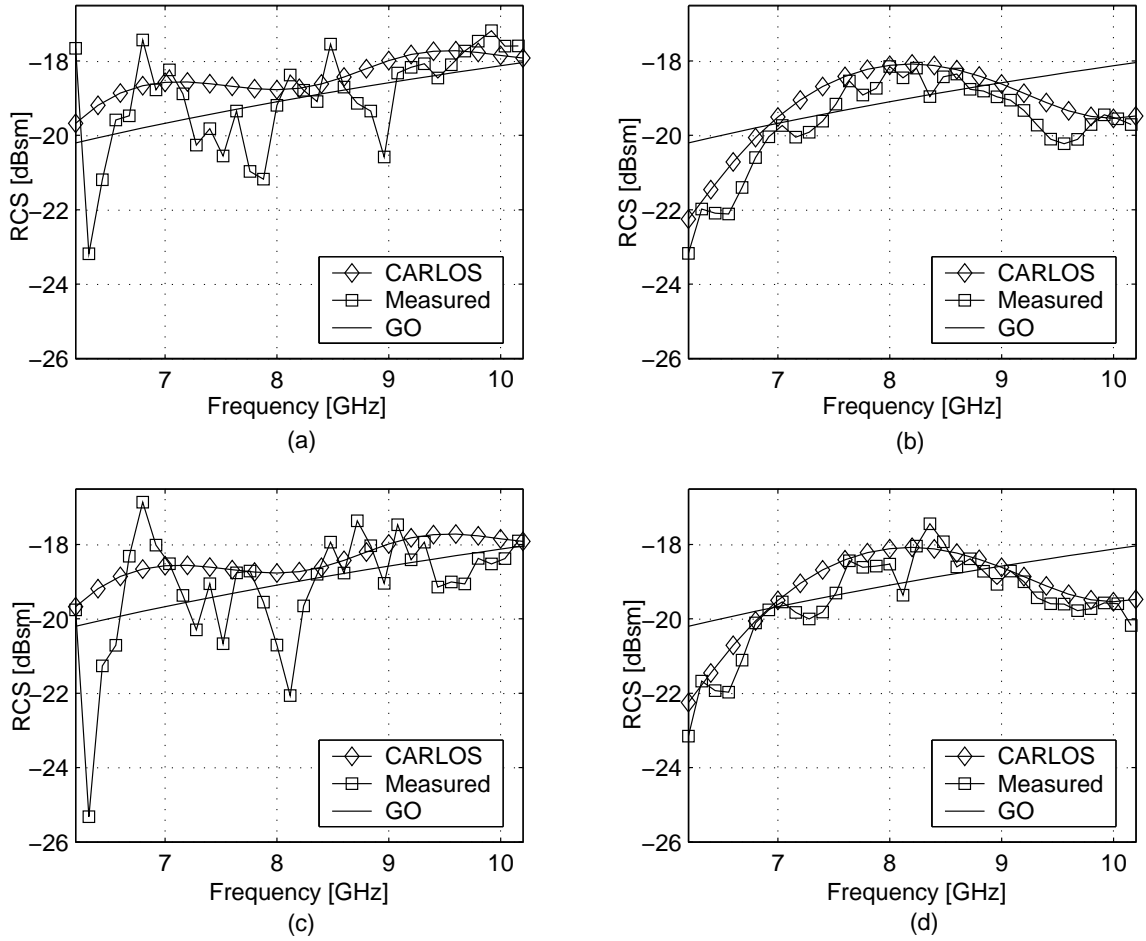


Figure 4.1: Simple two cylinder CARLOS, measured, and GO results for cylinder 1 and 2. (a) Cylinder 1 VV-polarization. (b) Cylinder 1 HH-polarization. (c) Cylinder 2, VV-polarization. (d) Cylinder 2 HH-polarization.

curved surface. However, there are additional contributions. Horizontal polarization (Figs. 4.1b and 4.1d) contributions are due to the creeping wave returns and diffraction from the rim edges. Additionally, the vertical polarization contributions are produced by surface traveling waves and diffraction from the rim edges. The surface traveling wave induces surface currents and produces a “sinusoidal” standing wave pattern resulting from the forward and reverse traveling waves created by the tip terminations. Figure 4.2 illustrates the surface currents on the cylinder in horizontal and vertical polarization at 6.2 GHz. The standing wave pattern in vertical polarization is evident in the plot as “hot spots” in the left-hand plot. The two “hot spots”

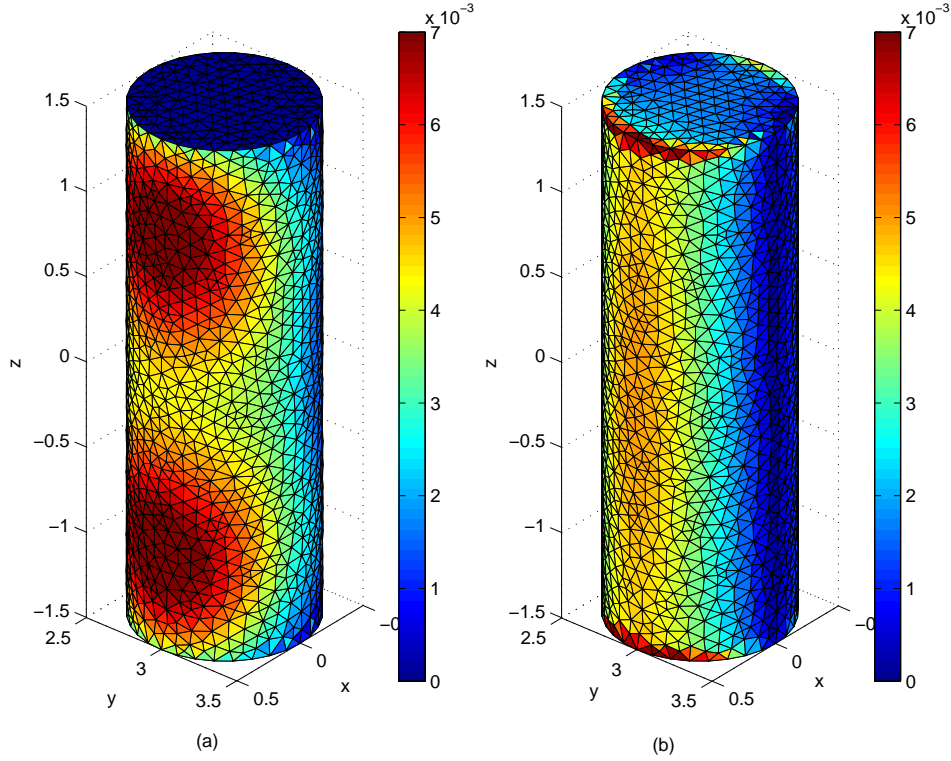


Figure 4.2: Surface Currents on Cylinder 2. (a) Verifies the standing wave in vertical polarization, which relates to a higher RCS in the Far-Field due to the specular scattering in addition to the standing wave on the surface. (b) Specular Scattering in Horizontal polarization which has a lower overall RCS due to the only contributor being the specular return in this polarization.

are representative of sinusoidal waveform peaks. Therefore, the separation distance should equate to one wavelength which at 6.2 GHz corresponds to approximately 1.9 inches. This agrees favorably with Fig. 4.2, where the center-to-center distance of the “hot spots” is 2 inches. Since the GO approximation only accounts for specular returns, intuitively the GO would predict lower RCS values for CARLOS or physical measurements. However, this is dependent on phase; which is dependent on fields constructively or destructively interfering. As shown in Fig.4.1, this holds true for vertical polarization, but in horizontal polarization it seems to hold true only over the band of 7 to 9 GHz.

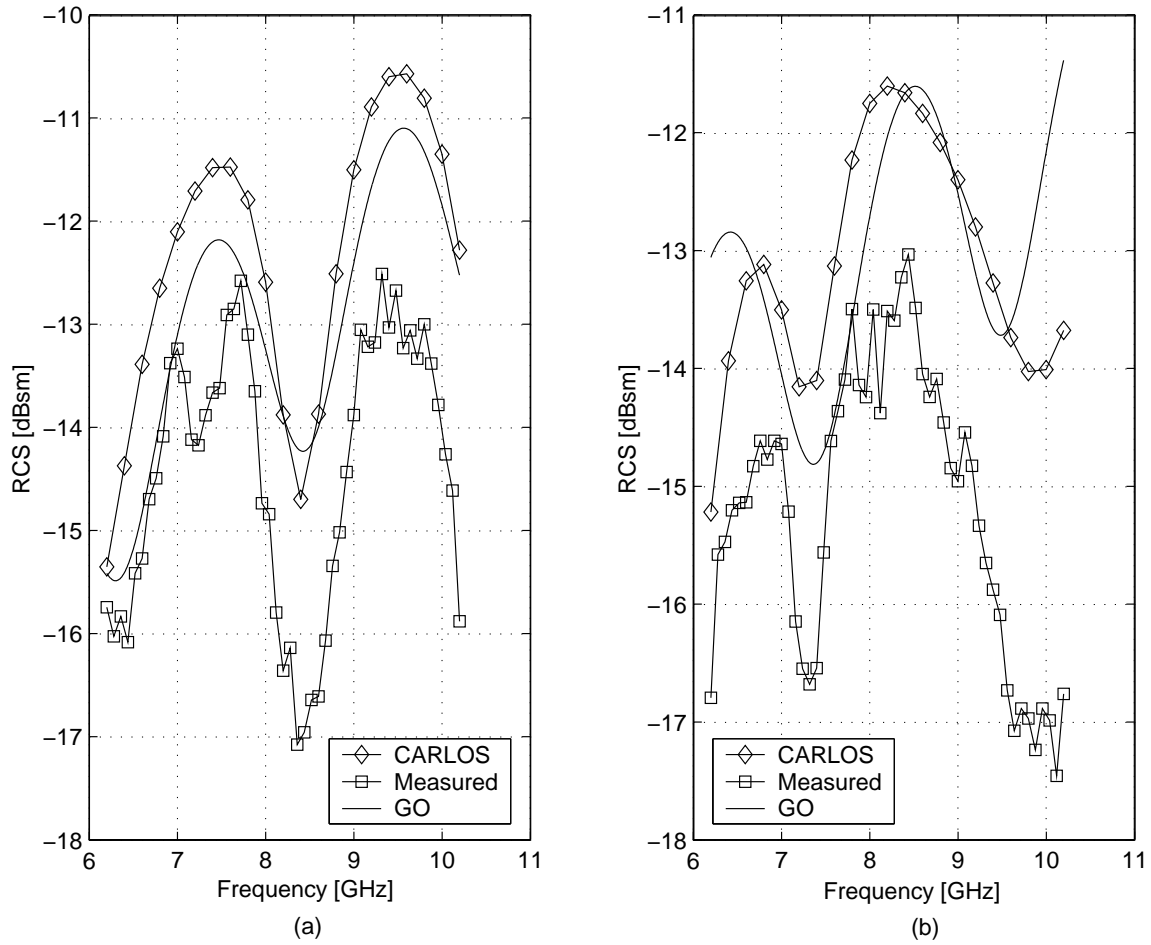


Figure 4.3: Simple two cylinder CARLOS, Measured, and GO results. (a) VV-polarization. (b) HH-polarization.

4.1.2 Combination of Cylinder 1 and 2. Attention is now turned to the two-cylinder configuration. The scattered field from this measurement is represented as \vec{E}_{tm}^s in Eqn. (3.4). The RCS results from the three techniques are depicted in Fig. 4.3. Measurements from the RCS range and the predictions from GO and CARLOS are in decent agreement and show similar trends. The GO analysis described in Sec 3.2.3 was carried out using only the “double bounce” and specular returns. Similar trends, i.e. peaks and valleys, among GO and CARLOS are prevalent. Since CARLOS accounts for traveling wave contributions, creeping waves, etc., the predicted results are in general higher. As expected, the lobing patterns between the three techniques

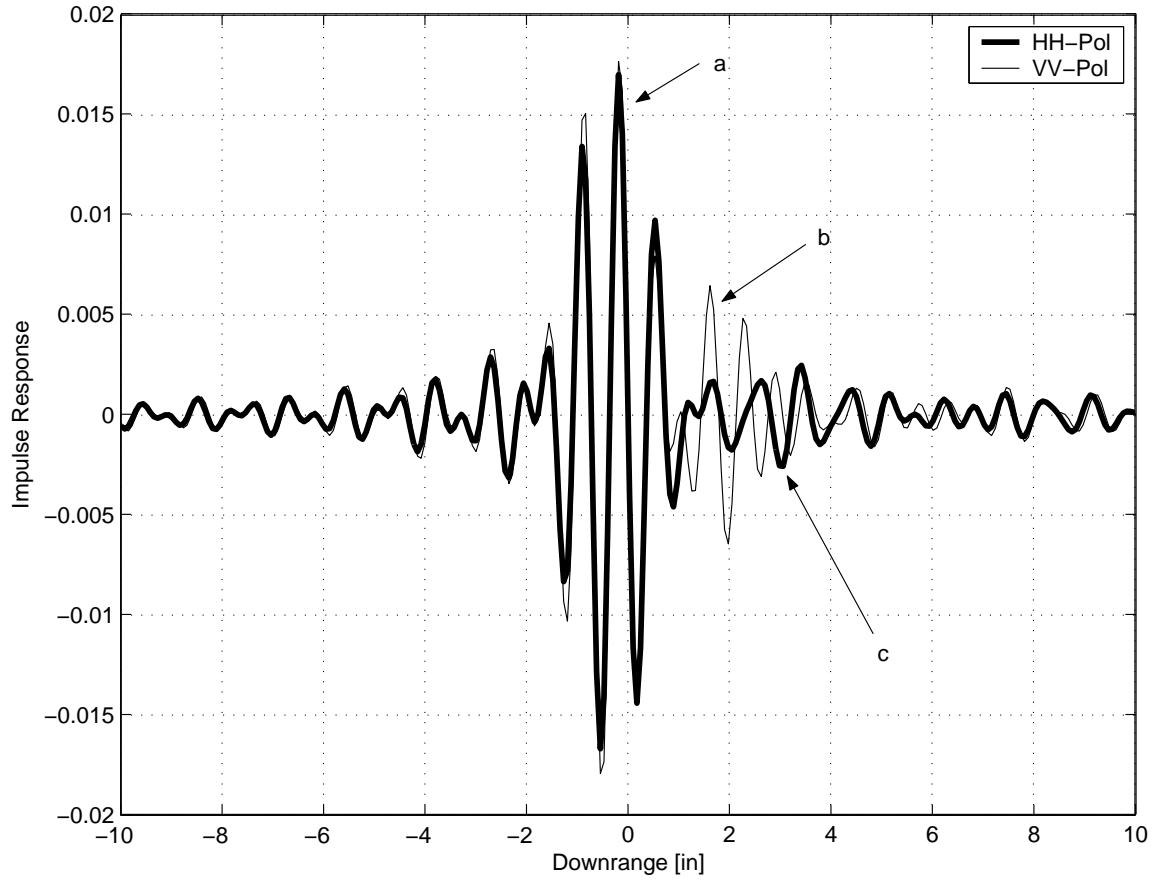


Figure 4.4: Downrange image of the two-cylinder configuration. (a) Specular Return apparent in both polarizations. (b) Contributions from diffraction off the back rim in VV-Pol. (c) Contributions from the creeping wave in HH-pol.

are in close agreement for both polarizations. Recall from Sec 3.1 that the scattered field due to the two-cylinder configuration contains the interaction between the cylinders. This can be visually represented by inverse Fourier Transforming the frequency domain data from the physical measurements to convert it to the time domain. This creates a downrange image of the cylinder's impulse response. Figure 4.4 depicts the downrange images of the two-cylinder configuration in horizontal and vertical polarization. The large impulse response at zero inches downrange (denoted by a) corresponds to the specular return from the cylinders. To relate the other impulse responses in the plot, several scattering mechanisms and their associated path length differences are taken into account. Consider the geometries in Fig. 4.5. Based on

Table 4.1: Scattering mechanisms and their downrange distances.

Scatt. Mech.	Down Range[in]	Ref. in Fig. 4.4	Ref. in Fig. 4.5
Specular Return	0.0	a	a1
Creeping Wave	1.3	c	a2
Diffraction from rim	1.0	b	b1
Diffraction around Cylinder	2.5	Indistinguishable	b2
“Double Bounce”	2.75	Indistinguishable	c

this geometry, the impulses can be attributed to the scattering mechanisms and their calculated downrange distances as summarized in Table 4.1. Several scattering mechanisms are listed as indistinguishable within the impulse response based on downrange *resolution* given by [2]

$$\Delta x = \frac{c}{2B} \quad (4.1)$$

where c is the speed of light in meters per second and B is the electrical bandwidth. For the bandwidth used here, *resolution* calculates to be approximately 1.5 inches. The resolution can be thought of as the minimum distance scatterers must be separated to be resolvable.

4.1.3 Isolation of the Interaction Between Cylinder 1 and 2. With completed measurements, both computational and physical, the isolation process can be validated using Eqn. (3.4) (repeated below).

$$\vec{E}_{int}^s = \vec{E}_{tm}^s - (\vec{E}_t^s + \vec{E}_m^s)$$

The fields are coherently subtracted and the results presented in Fig. 4.6. Comparing the computational to the physical measurement results, validate the isolation process, and also indicate a very important characteristic about the interaction term. As the frequency increases the electrical size of the cylinders increases. This is also true for the electrical distance between the cylinders. For example, at 6.2 GHz the

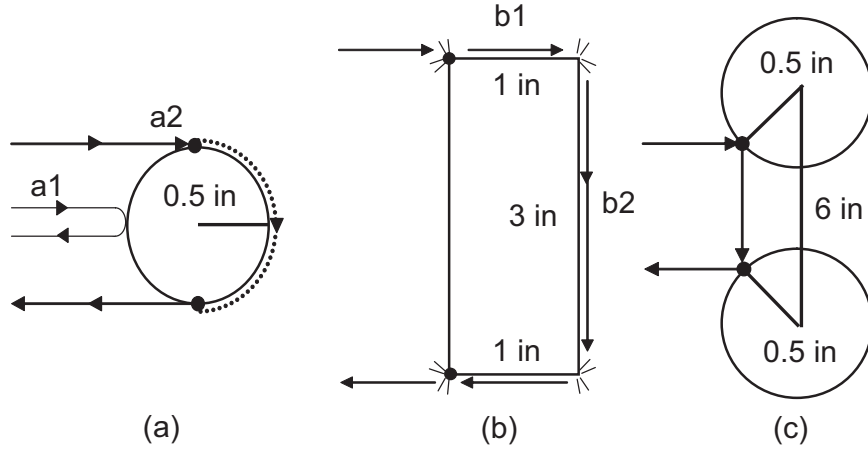


Figure 4.5: Geometrical path length differences. (a) Specular return apparent in both polarizations and creeping wave in horizontal polarization. (b) Contributions from diffracted fields traveling across the top of the cylinder, down the cylinder, and back across the bottom of the cylinder, apparent in VV-pol. (c) Contributions from the “double-bounce” in both polarizations.

wavelength is approximately 1.9 inches. Therefore, since the edge-to-edge distance of the cylinders is 5.0 inches, the cylinders are approximately 2.5 wavelengths apart. At 10.2 GHz the wavelength is approximately 1.2 inches and the electrical distance between the two cylinders increases to 5 wavelengths. As frequency continues to increase, so too does the electrical separation. This makes physical sense; as two object’s electrical separation continues to increase, the electromagnetic coupling (i.e. interaction) between the objects tends to decrease; electrical separation distance and interaction are inversely proportional. Overall, the predicted results from GO and CARLOS are corroborated through RCS measurements. Therefore, the isolation process can be utilized in a modified manner to tackle the problem of characterizing the interaction between the calibration targets and the ogive pylon.

4.2 Cylinder/Pylon Configuration

Results here are for the calibration target-ogive cross section pylon configuration. First, validation is performed for the Hertzian dipole approximation presented

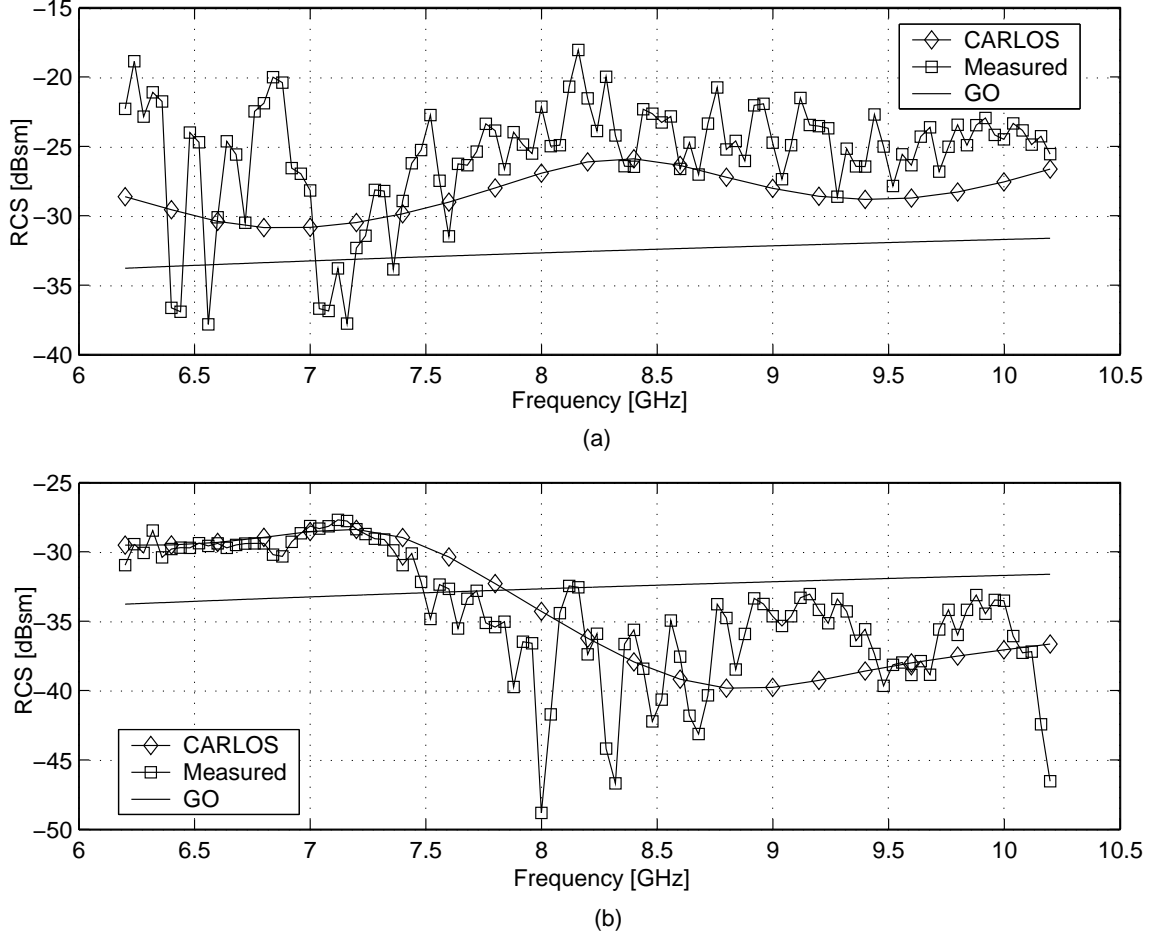


Figure 4.6: Simple Cylinder Computational, Measured, and GO results for the Interaction Scattering Mechanism. (a) VV-polarization. (b) HH-polarization.

in Sec. 3.3.2 for radiating the surface currents to the far-field. The results are then presented on the individual measurements needed in the isolation process, and finally the isolation process is carried out and the interaction is characterized. The analysis here involves computations with CARLOS only.

4.2.1 Validation of Hertzian Dipole Approximation. Section 3.3.2 described the process of extracting the far-field signature due to surface currents. Recall that the current on each facet was concentrated onto an equivalent Hertzian dipole and radiated to the far-field. Here we compare this method against results from CARLOS for the RCS of both calibration target-mount configurations. The results are

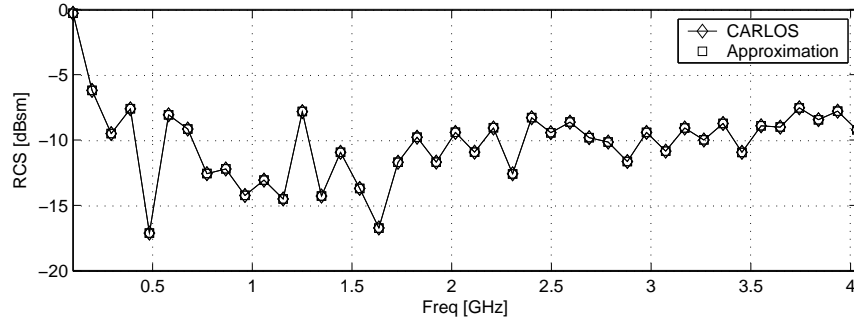


Figure 4.7: Validation of approximation on 1500x350 calibration target-mountain configuration VV-Polarization.

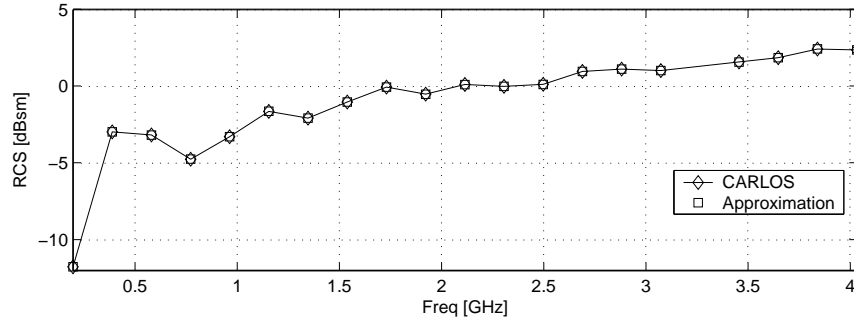


Figure 4.8: Validation of approximation on 1800x1200 calibration target-mountain configuration VV-Pol.

presented in Figures 4.7 and 4.8. The plots show the target-mountain configuration RCS between the outputs of the Hertzian dipole approximation and the CARLOS simulation. The plots indicate that the Hertzian dipole approximation is an accurate and viable approximation.

4.2.2 Results for Calibration Targets. The following section describes results for the 1500x350 and 1800x1200 calibration target that scatters the field \vec{E}_t^s for the isolation process. Although this measurement may not be physically realizable, simulated results are used to characterize the interaction between the calibration target-mountain configuration. Figure 4.9 depicts the triangular mesh utilized by CARLOS to find the surface currents for the calibration targets. Once the surface currents are known, the far zone fields are found utilizing the process in Sec 3.3.2 to

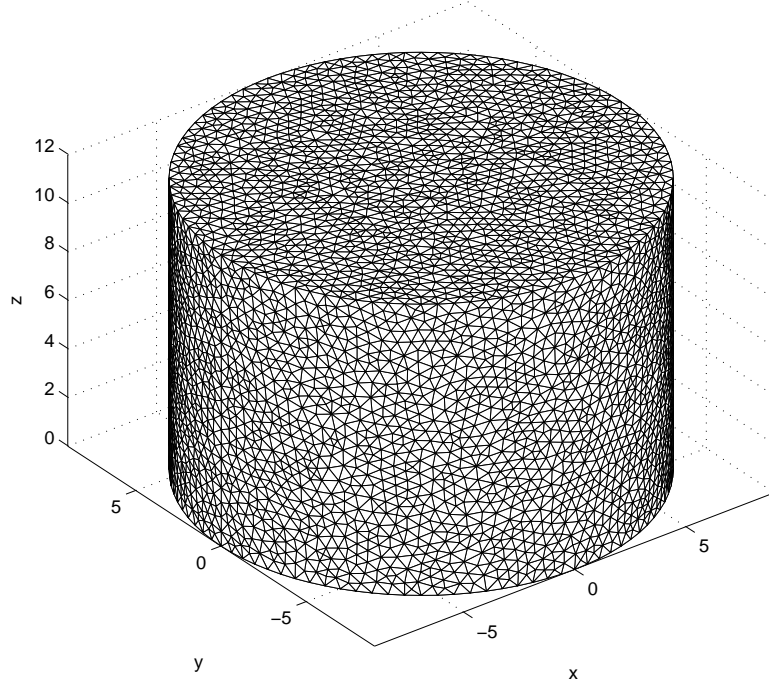


Figure 4.9: Triangular mesh for the calibration target utilized within CARLOS. 1800x1200 Cylinder.

obtain \vec{E}_t^s . The physical target dimensions consisted of a 15-inch diameter by 3.5-inch height for the 1500x350 cylinder and an 18-inch diameter by 12-inch height for the 1800x1200 cylinder. The computation consisted of a monostatic frequency sweep from 4 MHz to 4.003 GHz in 96 MHz increments, at an aspect of $\theta = 90^\circ$ and $\phi = 0^\circ$, in vertical and horizontal polarizations. The angular orientation replicates typical calibration measurements. Figure 4.10 shows the RCS of both calibration targets for horizontal and vertical polarization. Similar to the results obtained in the simple two cylinder geometry, the overall target RCS of the targets is relatively independent of polarization except at lower frequencies. The polarization independence may be partly due to the dominant specular scattering mechanism.

4.2.3 Cylinder Mounted on Pylon. As stated in the isolation process of Sec. 3.1, the scattered field due to the mount alone (\vec{E}_m^s) is not measurable in the

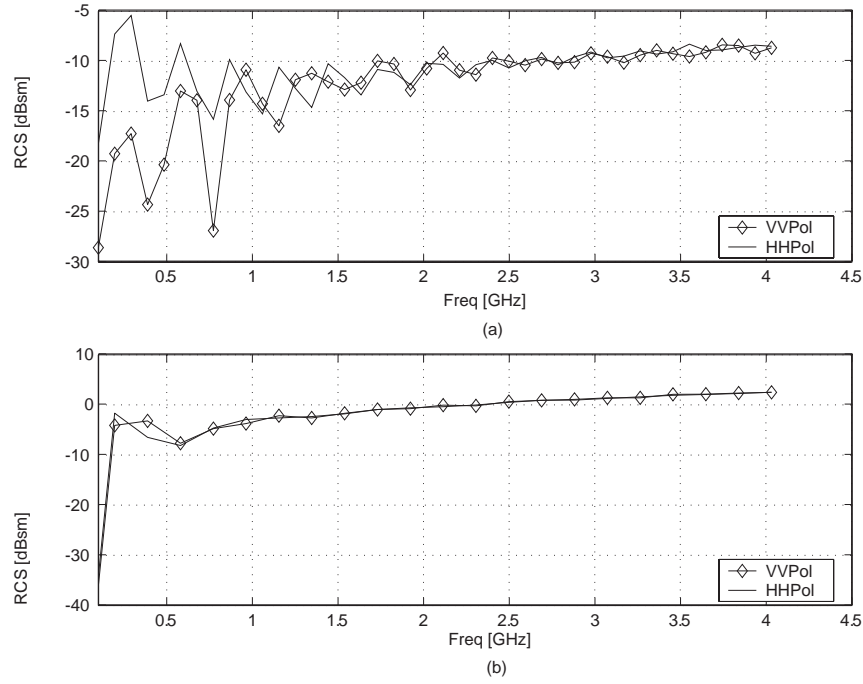


Figure 4.10: Frequency sweep computations for the 1500x350 and 1800x1200 calibration targets. (a) 1500x350 Cylinder VV- and HH-Pol. (b) 1800x1200 VV- and HH-Pol.

calibration target and mount configuration. The reasoning is simple; in the target-mount configuration the top of the ogive cross section pylon is shadowed, but when the mount is measured alone, the top of the pylon is visible to the radar. Therefore, a modified version of the isolation process, described in Sec. 3.3.2 is used to extract currents on the surface of the ogive cross section pylon in the *presence* of the calibration targets. Then those currents are radiated to the far-field to obtain a true representation of the contributions due to the mount alone. Figure 4.11 depicts the mesh utilized for the 1800x1200 targets within CARLOS to obtain the surface currents. The RCS of the mount alone is not presented. However, the fields radiated by the currents on the mount (\vec{E}_m^s) are utilized in isolating the interaction. The RCS of the target-mount configuration is presented. Figure 4.12 depicts the RCS of both calibration target-mount configurations in vertical and horizontal polarization. The target-mount scattered field (\vec{E}_{tm}^s) in this configuration is included in the

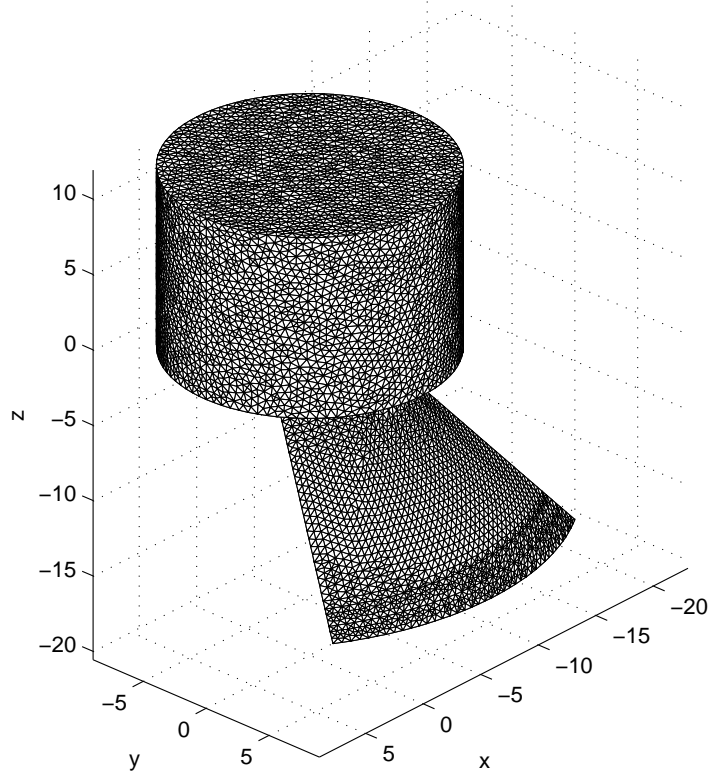


Figure 4.11: Meshed Geometry for the calibration target-mount configuration utilized with CARLOS to obtain the surface currents. 1800x1200 Calibration Target-Mount Configuration.

isolation process. The RCS of the target-mount configuration indicates interesting characteristics of the ogive cross section pylon. By comparing the overall RCS levels in Fig. 4.10 with Fig. 4.12, the pylon can be characterized as an extremely low RCS target. However, the \vec{E}_m^s scattered field incorporates the interaction term. The interaction can now be isolated since all measurements are available to carry out the isolation process.

4.2.4 Isolation of the Interaction in the Calibration Target-Mount Configuration. The isolation process for the calibration target-mount configuration is presented in a similar fashion as the simple two-cylinder geometry. That is, the RCS

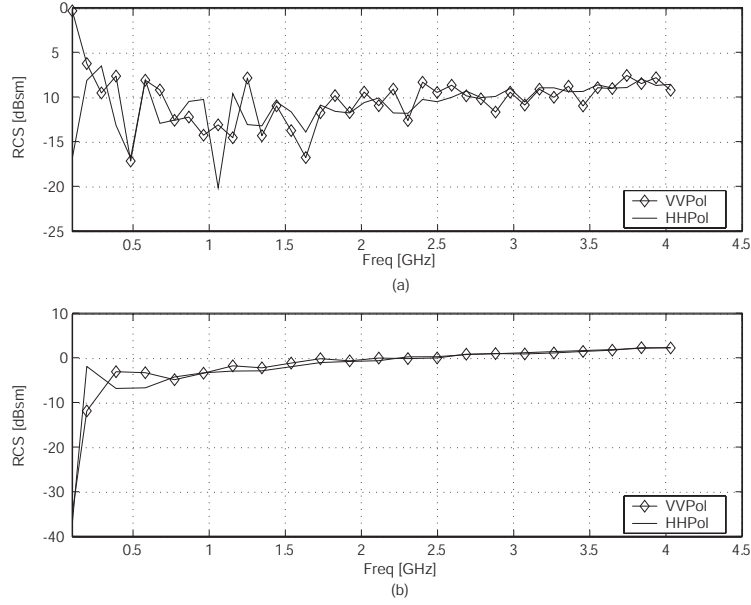


Figure 4.12: RCS of: (a) 1500x350 calibration target-mount configuration and (b) 1800x1200 calibration target-mount configuration.

of the interaction is presented as a function of frequency. Again, once the measurements \vec{E}_{tm}^s , \vec{E}_t^s , and \vec{E}_m^s , have been obtained computationally or through extraction, the interaction term \vec{E}_{int}^s can be extracted from \vec{E}_{tm}^s . The interaction term for both calibration targets in vertical and horizontal polarizations are presented in Fig. 4.13. Based on the RCS levels, the interaction in the 1500x350 calibration target-mount configuration (Fig. 4.13a) is significantly less (approximately -30 dB) than the RCS of the target-mount configuration (Fig. 4.12a). This implies the interaction effects are extremely low, allowing the returns to be neglected. Similar results are obtained for the 1800x1200 calibration target-mount configuration. The following section, utilizes the extraction process described in Sec. 3.3.2 and evaluates the “difference” currents on the surface of the calibration targets *with* and *without* the pylon present. The purpose of the following section is to gain insight into, and characterize, the interaction.

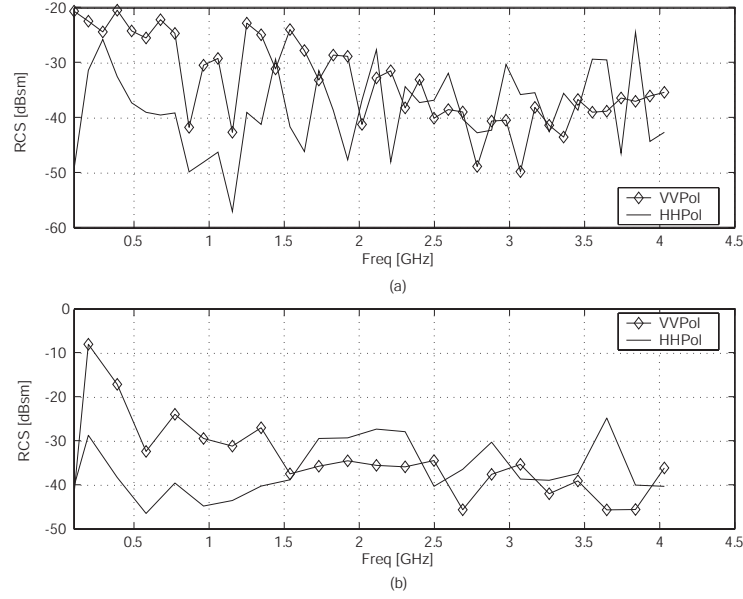


Figure 4.13: RCS of interaction in: (a) 1500x350 calibration target-mount configuration and (b) 1800x1200 calibration target-mount configuration.

4.2.5 Difference Currents on the Surface of the Calibration Targets. The purpose of this section is to determine the effects on the target with and without the pylon present. From a macro perspective, if the currents are coherently subtracted, the difference if radiated to the far-field is the interaction term described in the previous section. Fig. 4.14 and Fig. 4.16 shows the pylon effects on the 1800x1200 calibration target in vertical and horizontal polarization, respectively. The plots depict the surface currents of the target simulated alone, in the presence of the pylon, and the “difference currents” on the surface of the target at the lowest, middle, and highest frequency simulated. The plot depicted in Fig.4.14a is indicative of frequency effects on the interaction term in VV-pol. At the lowest frequency of 196 MHz, the “difference” cylinder shows an extremely high amount of coupling on the base of the cylinder. At 196 MHz, the target (18 inches) is electrically small compared to a wavelength (60 inches), and therefore the effects of coupling is strongest. Another interesting characteristic of the cylinder extracted from the target-mount configuration is that at low frequencies the specular flash off the front

of the cylinder is not the dominant scattering mechanism, the interaction between the target and pylon is, though.

Figure 4.14b represents the middle frequency of 2.115 GHz simulated in CARLOS. The standing wave pattern illustrates a full cycle, which agrees well with the approximate 6 inch wavelength. The cylinder that signifies the difference currents on the surface illustrates that as the frequency increases the target becomes electrically smaller, and therefore the interaction between the target-pylon also decreases.

Finally at the highest frequency simulated, 4.033 GHz, the difference currents on the surface of the cylinder indicate an extremely low interaction. Specular returns from the cylinder surface provides the largest contribution. The four complete cycles that the standing waves progress through agrees well with the approximate 3 inch wavelength at 4.033 GHz.

Overall, Fig. 4.14 illustrates the frequency effects on the target-pylon interaction in VV-pol. The interaction becomes more prevalent when the surface cylinder currents are radiated to the far-field. Figure 4.15 highlights the interaction-frequency relationship. In general, the plot indicates that at low frequencies in VV-pol, where the target is electrically small, the interaction is significant and may not be neglected. However, when the target becomes electrically large (higher frequencies), the interaction is less significant and may possibly be neglected without degrading overall RCS measurements. To account for the interaction at the lower frequencies the frequency sweep measurements created for the interaction can be used in conjunction with the modified vector background subtraction equation, Eqn. (1.3), to obtain a more accurate representation of the target's RCS.

The plot depicted in Fig.4.16a is indicative of frequency effects on the interaction term in HH-pol at the lowest frequency sampled of 196 MHz. The plot indicates that overall there is a low level of interaction.

Figure 4.16b represents the middle frequency of 2.115 GHz simulated in CARLOS. At this frequency the interaction seems to show some strange anomalies. Further investigation, that is radiating to the far-field, must be carried out to fully understand what is occurring.

Finally at the highest frequency simulated, 4.033 GHz, the difference currents on the surface of the cylinder indicate an extremely low interaction.

Overall, Fig. 4.16 illustrates the frequency effects on the target-pylon interaction in HH-pol. The interaction becomes more prevalent when the surface cylinder currents are radiated to the far-field. Figure 4.17 highlights the interaction-frequency relationship. The anomalies that are evident in the mid-frequencies could possibly be a resonance issue and could be further investigated by looking that the solution using the Combined Field Integral Equation. In general, though, the plot indicates that in HH-pol the interaction is minimal and can be neglected without degrading the overall RCS measurements.

From a physical stand-point it makes sense that the interaction is strongest in VV-pol due to the induced currents on the knife edge of the pylon, which in turn creates a “pile up” of charge at the termination of the pylon. This charge then radiates and interaction can become most significant. However, in HH-pol the traveling waves that “wrap” around the ogive cross section shed energy while traversing the surface of the pylon, therefore the build up of charge is less significant on the trailing knife edge which equates to a less significant interaction.

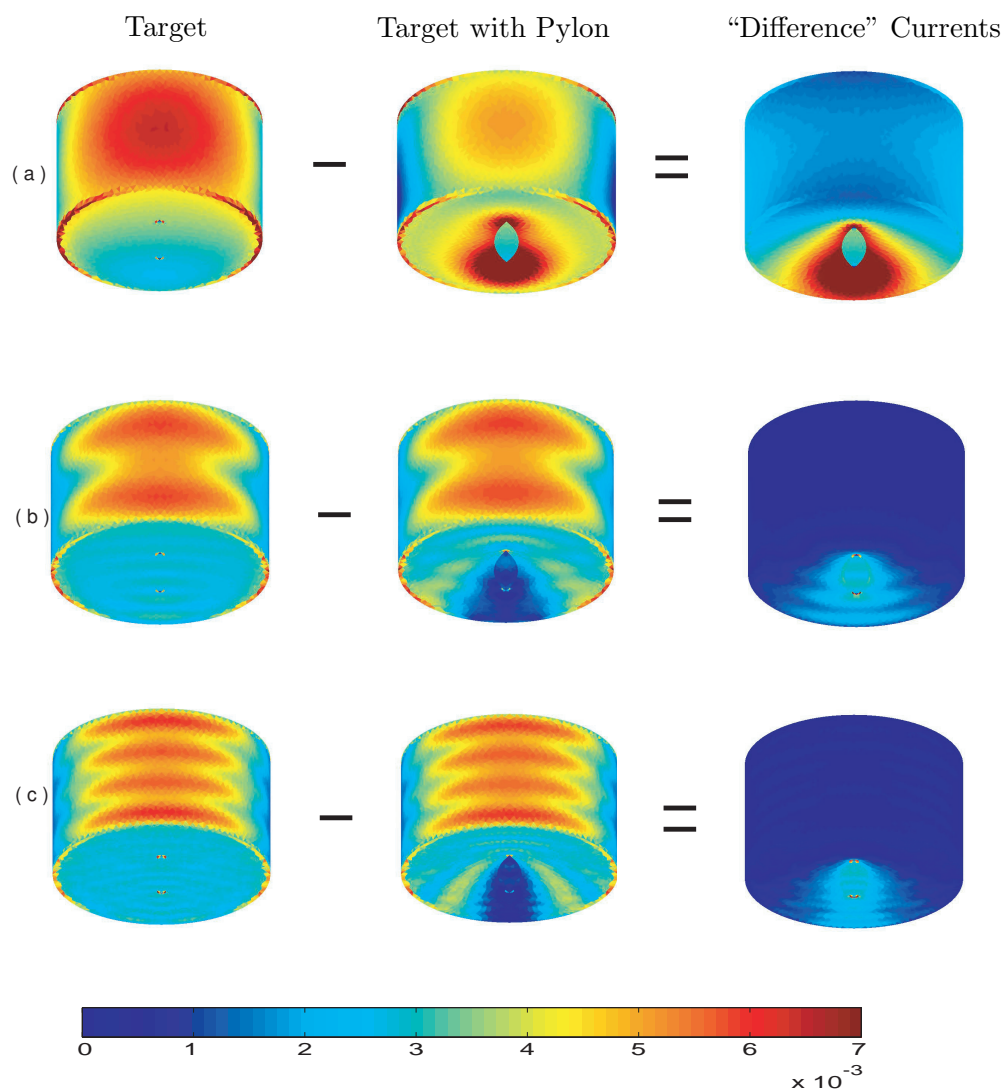


Figure 4.14: Surface Currents on the 1800x1200 calibration target, VV-pol: (a) Frequency: 196 MHz (b) Frequency: 2.1150 GHz (c) 4.033 GHz

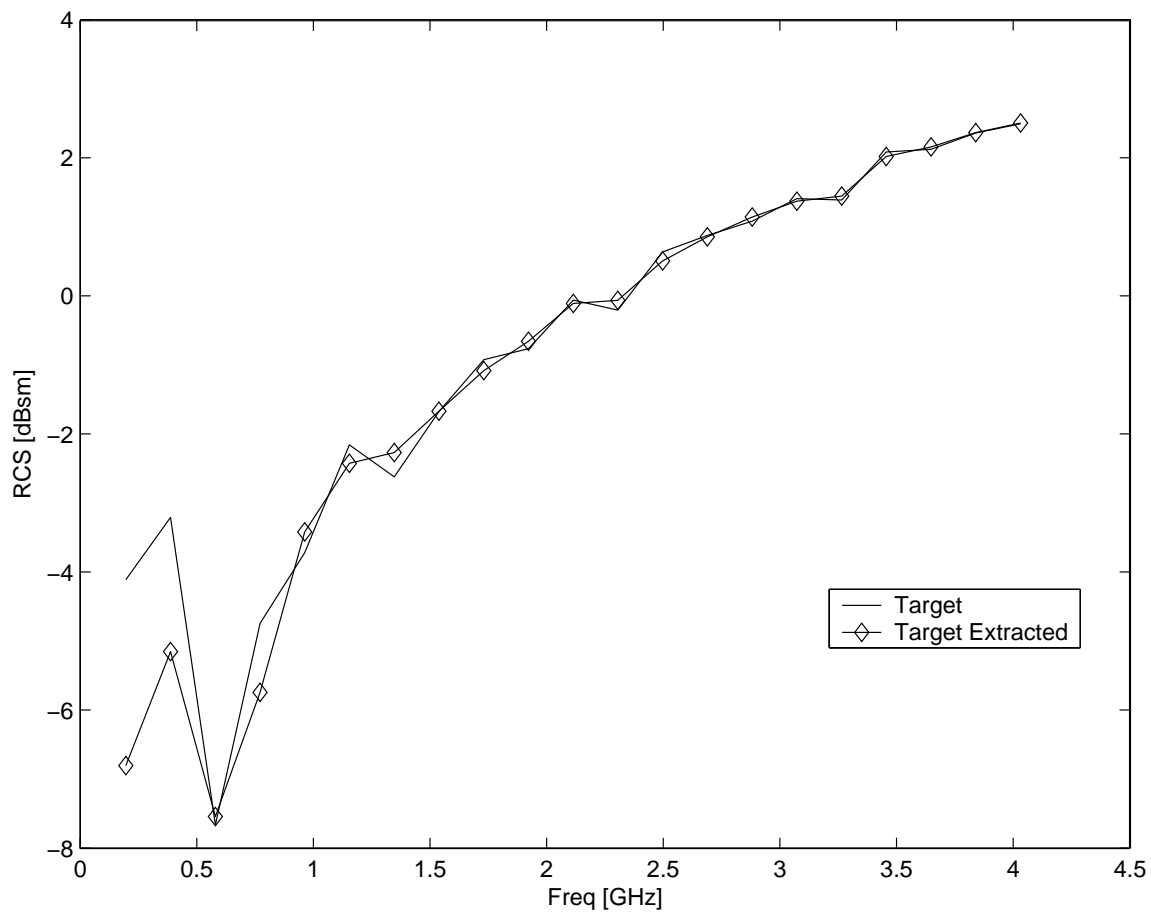


Figure 4.15: RCS of target in the presence and absence of the pylon in VV-Pol. Plot indicates that as the target becomes electrically large (increasing frequency) the interaction becomes relatively small.

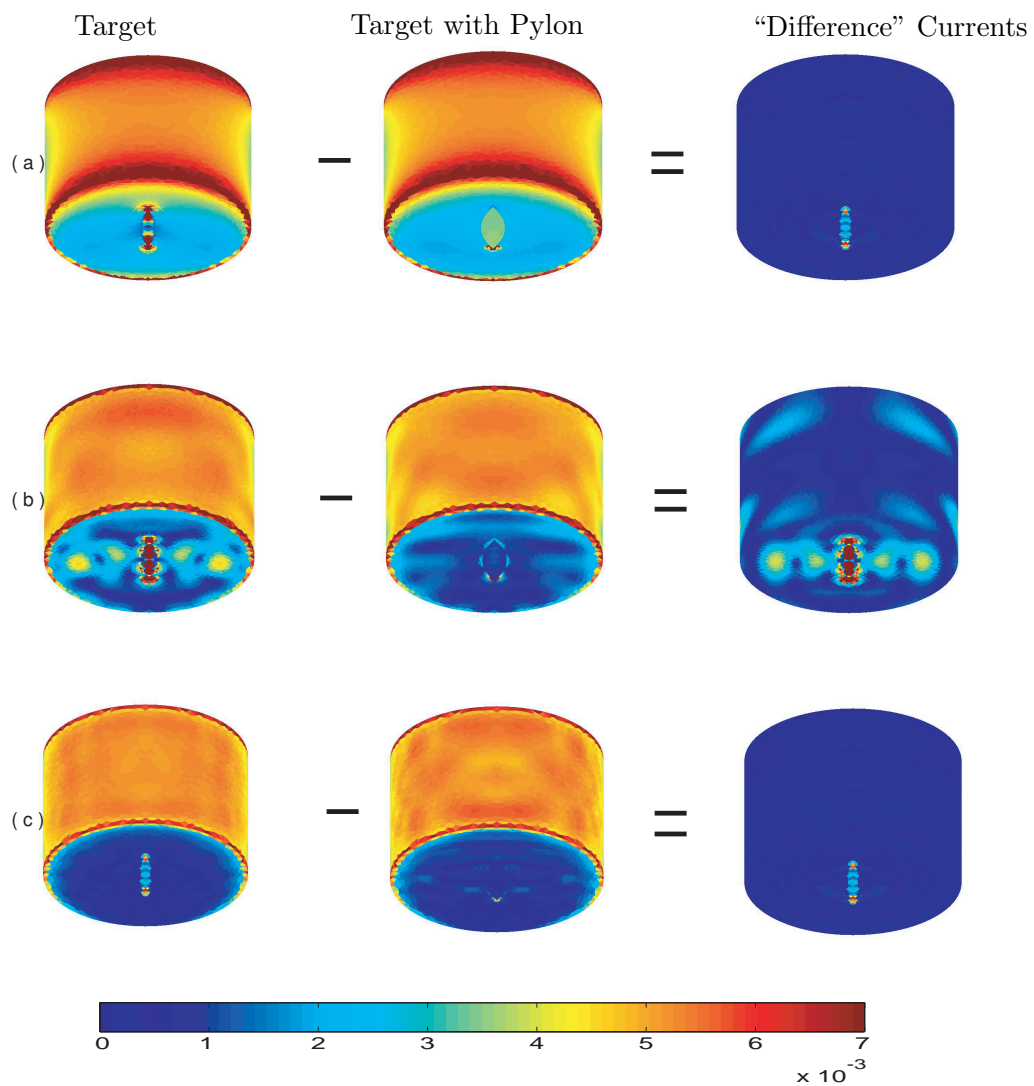


Figure 4.16: Surface Currents on the 1800x1200 calibration target, HH-pol: (a) Frequency: 196 MHz (b) Frequency: 2.1150 GHz (c) 4.033 GHz

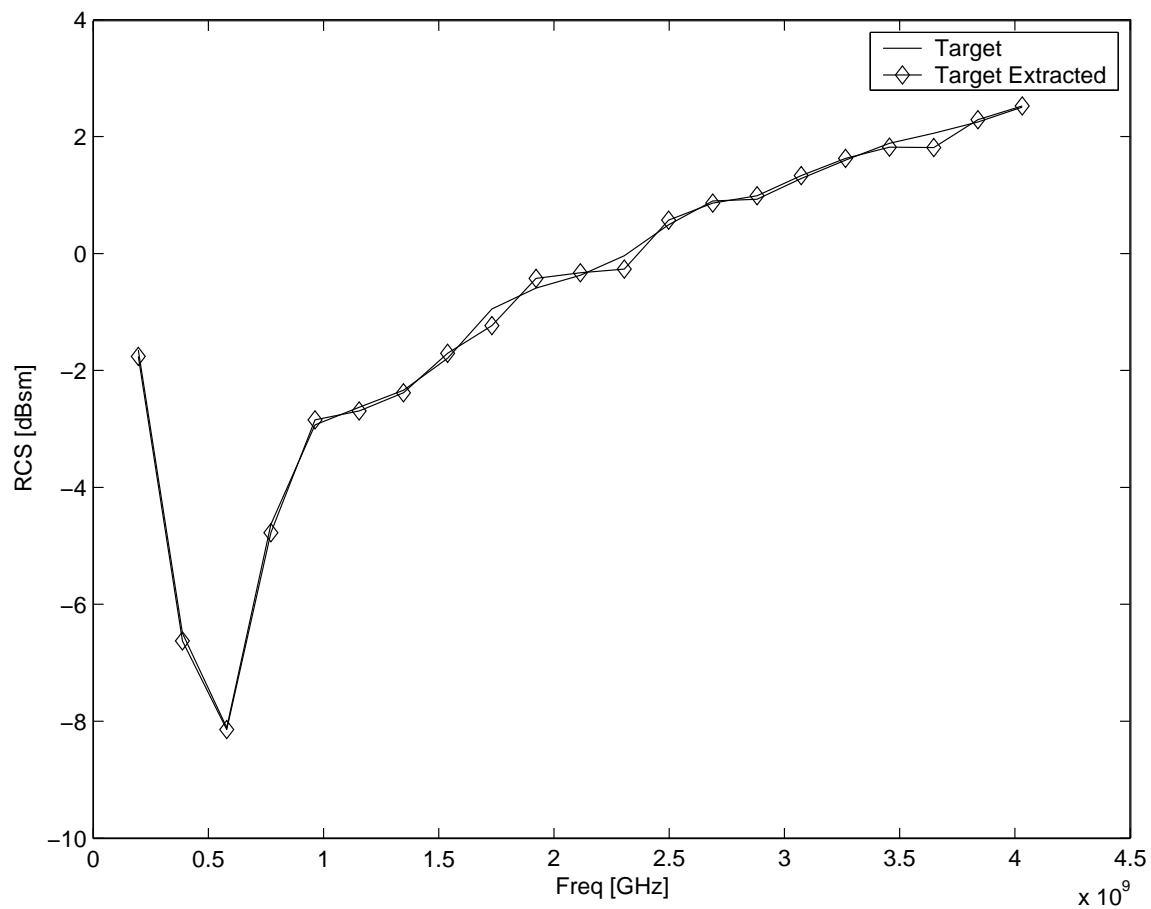


Figure 4.17: RCS of target in the presence and absence of the pylon in HH-Pol. Plot indicates that in general interaction is negligible in HH-Pol.

V. Conclusions and Future Work

Throughout this research the ultimate goal was to characterize the interaction in Radar Cross Section (RCS) calibration measurements to obtain a modified vector background subtraction formula that accounts for the interaction. The contents of this chapter present the overall conclusions based on the results of Chapter IV.

5.1 Conclusions

The thesis was divided up into two sections: a simple two cylinder geometry to validate the process of isolation, and the 1500x350 and 1800x1200 calibration target-mount configuration to characterize the interaction.

5.1.1 Conclusions on Simple Two Cylinder Geometry. The process of isolation involved the coherent subtraction of scattered fields due to the target, the mount, and target-mount configuration in an RCS measurement. Measurements were taken in AFIT's RCS Range on a simple two cylinder geometry, and validated against both a 3-dimensional Method of Moments code CARLOS and the high frequency Geometric Optics technique. The computational techniques corroborate the measurements. Therefore, using the isolation interaction process is a valid technique. More generally, it can be utilized to isolate the interaction between multiple scatterers.

5.1.2 Conclusions on Calibration Target-Mount Configuration. Upon conducting further research it was determined that the isolation process utilized on the simple two cylinder geometry provides a concise process for obtaining the interaction. However, it does not account for shadowing of the mount by the target in RCS measurements. In practice, in a pylon/rotator configuration, the mount is never measured alone. Therefore, a modified version of the isolation process was developed using the surface currents provided by CARLOS. This new method involves

extracting currents associated with a given surface and radiating to the far-field. The method was validated against results from CARLOS. Moving on, the extraction process was utilized to obtain the RCS of the interaction by carrying out the coherent subtraction process on fields extracted from the calibration target-mount configuration. Through this process several general conclusions are made regarding the interaction in calibration measurements, including:

- The interaction is target dependent
- The interaction is more apparent in the VV-polarization than HH-polarization
- The interaction is a function of electrical size. For targets that are electrically small, or on the same order of magnitude as a wavelength, the interaction between the target-pylon is significant. However, when the target becomes electrically large the interaction decrease and can be considered negligible.
- To account for the interactions at lower frequencies, interaction frequency sweeps (similar to the plots in Fig. 4.13) can be utilized in conjunction with the modified vector background subtraction equation given by

$$\sigma_{tgt} = \frac{|\vec{E}_{tgt}^s - \vec{E}_{bkg}^s|^2}{|\vec{E}_{cal}^s - \vec{E}_{cbk}^s - \vec{E}_{cint}^s|^2} \sigma_{cal}$$

to obtain a more accurate RCS of the target under consideration.

5.2 Future Work

Since this was the first of what hopes to be many endeavors into the characterization of the target-mount interaction, several other areas can be pursued to provide a better understanding of the interaction scattering mechanism. Other areas for further study include:

- Classification of calibration targets based on their interaction with the pylon. This could include creating a graphical user interface to provide the user with

tools for determining the interaction based on the calibration target of their choice.

- Modelling an actual RCS range ogive-pylon and determining the dependence on the interaction by varying the pylon length.
- Application of surface treatments to mitigate returns from the pylon termination.
- Extension of the extraction process to include other angular orientations.
- Simulation of foam mounts to gain insight on the interaction scattering mechanism.
- Extend process to look at targets to include an additional term in the numerator of modified vector background subtraction which will take the form,

$$\sigma_{tgt} = \frac{|\vec{E}_{tgt}^s - \vec{E}_{bkg}^s - \vec{E}_{tint}^s|^2}{|\vec{E}_{cal}^s - \vec{E}_{cbk}^s - \vec{E}_{cint}^s|^2} \sigma_{cal}$$

Appendix A. Geometric Optics Analysis

This appendix describes the Geometric Optics (GO) analysis to obtain the scattered fields presented in Sec. 3.2.3. The analysis is carried out two dimensionally, followed by a two-dimensional to three-dimensional transformation to obtain the RCS of the GO fields. [1] was used throughout this derivation.

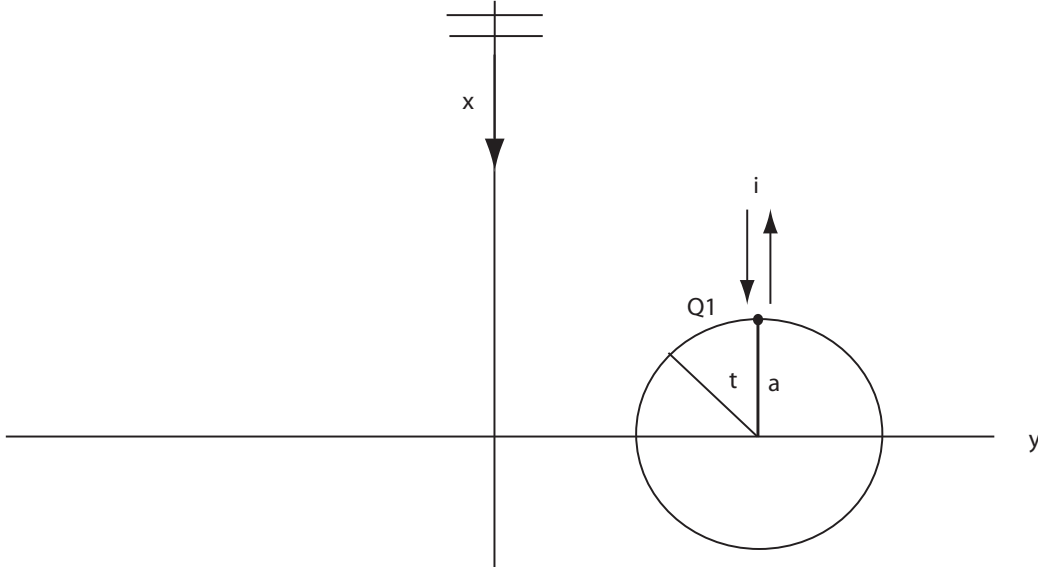


Figure A.1: Single Cylinder Geometry

A.1 Single Cylinder Derivation

Begin with the single cylinder return VV-pol or soft polarization.

$$\vec{E}^i = \hat{z} E_o e^{-j\vec{k} \cdot \vec{r}} \quad (\text{A.1})$$

where $\vec{k} = -k_o \hat{x}$, $\vec{r} = \hat{x}x + \hat{y}y \Rightarrow \vec{k} \cdot \vec{r} = -k_o x$, and

$$\vec{E}^i = \hat{z} E_o e^{jk_o x} \quad (\text{A.2})$$

The incident wave at the point Q_1 then becomes

$$\vec{E}^i(Q_1) = \hat{z}E_o e^{jk_o x(Q_1)} \quad (\text{A.3})$$

where $x(Q_1) = a \cos \theta$. For this research $\theta = 0$ radians $\Rightarrow x(Q_1) = a$, and

$$\vec{E}^i(Q_1) = \hat{z}E_o e^{jk_o a} \quad (\text{A.4})$$

$$\vec{E}_{t,m}^s = \vec{E}^i(Q_1)(-1)\sqrt{\frac{\rho_1}{\rho_1 + s_1}} e^{-jk_o s_1}$$

since $S_1 = R - a \cos \theta$, as $\cos \theta \rightarrow 1$, $s_1 = R - a$, and

$$\begin{aligned} \vec{E}_{t,m}^s &= -\hat{z}E_o e^{jk_o a} \sqrt{\frac{\rho_1}{\rho_1 + s_1}} e^{-jk_o s_1} \\ &= -\hat{z}E_o e^{jk_o a} \sqrt{\frac{\frac{a}{2}}{\frac{a}{2} + R - a}} e^{-jk_o s_1} \\ &= -\hat{z}E_o e^{jk_o a} \sqrt{\frac{a}{a + 2R - 2a}} e^{-jk_o s_1} \\ &= -\hat{z}E_o e^{jk_o a} \sqrt{\frac{a}{2R - a}} e^{-jk_o s_1} \end{aligned} \quad (\text{A.5})$$

one final substitution produces

$$\text{where } R \rightarrow \infty \vec{E}_{t,m}^s \simeq -\hat{z}E_o e^{jk_o 2a} \sqrt{\frac{a}{2}} \frac{e^{-jk_o R}}{\sqrt{R}} \quad (\text{A.6})$$

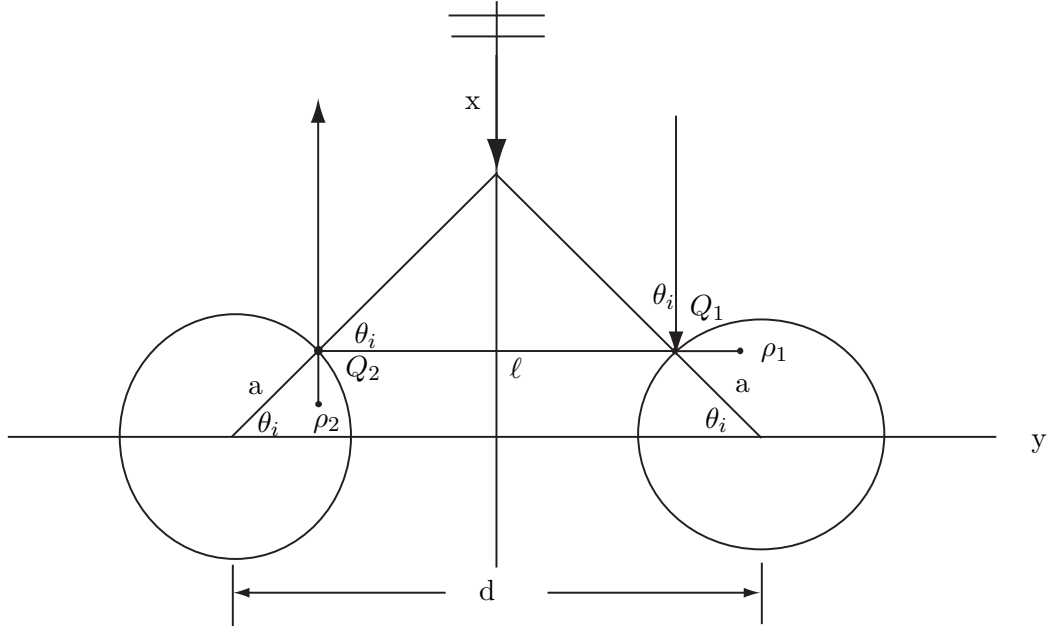


Figure A.2: Two-Cylinder Geometry

A.2 “Double Bounce” Derivation

Analysis of the two-cylinder geometry requires the calculation of three fields;

1. The field incident upon Q_1
2. The field incident upon Q_2 emanating from Q_1
3. The field radiating from Q_2 out to $R \rightarrow \infty$

The field incident upon Q_1 is

$$\vec{E}^i(Q_1) = \hat{z} E_o e^{jk_o a \sin \theta_i} \quad (\text{A.7})$$

The field incident upon Q_2 emanating from Q_1 is defined as

$$\begin{aligned}
\vec{E}^i(Q_2) &= \vec{E}^i(Q_1)(-1)\sqrt{\frac{\rho_1}{\rho_1 + s_1}} e^{-jk_o s_1} \text{ where } \rho_1 = \frac{a \cos \theta_i}{2} \text{ and } s_1 = \ell \\
&= -\hat{z} E_o e^{jk_o a \sin \theta_i} \sqrt{\frac{\frac{a \cos \theta_i}{2}}{\frac{a \cos \theta_i}{2} + \ell}} e^{-jk_o \ell} \\
&= -\hat{z} E_o e^{jk_o(a \sin \theta_i - \ell)} \sqrt{\frac{a \cos \theta_i}{a \cos \theta_i + 2\ell}}
\end{aligned} \tag{A.8}$$

The field radiating from Q_2 out to $R \rightarrow \infty$ is

$$\vec{E}_{int}^s = \vec{E}^i(Q_2)(-1)\sqrt{\frac{\rho_2}{\rho_2 + s_2}} e^{-jk_o s_2}, \quad s_2 = R - a \sin \theta_i \tag{A.9}$$

from [1]

$$\begin{aligned}
\frac{1}{\rho_2} &= \frac{1}{\rho_0} + \frac{2}{a \cos \theta_i} \\
&= \frac{1}{\rho_1 + S_1} + \frac{2}{a \cos \theta_i} \\
&= \frac{1}{\frac{a \cos \theta_i}{2} + \ell} + \frac{2}{a \cos \theta_i} \\
\Rightarrow \rho_2 &= \frac{(a \cos \theta_i + 2\ell)a \cos \theta_i}{4(a \cos \theta_i + \ell)}
\end{aligned} \tag{A.10}$$

substitution creates

$$\begin{aligned}
\vec{E}_{int} &= \vec{E}^i(Q_2)(-1)\sqrt{\frac{\rho_2}{\rho_2 + s_2}} e^{-jk_o s_2} \\
&= -\hat{z} E_o e^{jk_o(a \sin \theta_i - \ell)} \sqrt{\frac{a \cos \theta_i}{a \cos \theta_i + 2\ell}} \sqrt{\frac{\frac{(a \cos \theta_i + 2\ell)a \cos \theta_i}{4(a \cos \theta_i + \ell)}}{\frac{(a \cos \theta_i + 2\ell)a \cos \theta_i}{4(a \cos \theta_i + \ell)} + (R - a \sin \theta_i)}} e^{-jk_o(R - a \sin \theta_i)}
\end{aligned}$$

which simplifies to

$$= -\hat{z} E_o e^{jk_o(2a \sin \theta_i - \ell)} \sqrt{\frac{(a \cos \theta_i)^2}{4(a \cos \theta_i + \ell)}} \frac{e^{-jk_o R}}{\sqrt{R}} \tag{A.11}$$

Scattered field two-cylinder configuration

$$\begin{aligned}
E_{tm}^s &= 2\vec{E}_{int}^s + 2\vec{E}_{t,m} \\
&= \left[2\hat{z}E_o e^{jk_o(2a \sin \theta_i - \ell)} \sqrt{\frac{(a \cos \theta_i)^2}{4(a \cos \theta_i + \ell)}} - 2\hat{z}E_o e^{2jk_o a} \sqrt{\frac{a}{2}} \right] \frac{e^{-jk_o R}}{\sqrt{R}} \\
&= 2\hat{z}E_o \left[e^{jk_o(2a \sin \theta_i - \ell)} \sqrt{\frac{(a \cos \theta_i)^2}{4(a \cos \theta_i + \ell)}} - e^{2jk_o a} \sqrt{\frac{a}{2}} \right] \frac{e^{-jk_o R}}{\sqrt{R}} \\
|E_{tm}^s|^2 &= \frac{4E_o^2}{R} \left| e^{jk_o(2a \sin \theta_i - \ell)} \sqrt{\frac{(a \cos \theta_i)^2}{4(a \cos \theta_i + \ell)}} - e^{2jk_o a} \sqrt{\frac{a}{2}} \right|^2
\end{aligned} \tag{A.12}$$

A.3 RCS Calculations

A.3.1 $\vec{E}_{t,m}^s$ RCS Calculation.

$$|\vec{E}_{t,m}^s|^2 = \frac{E_o^2 a}{R} \tag{A.13}$$

where $E_o^2 = |\vec{E}^i|^2$

$$\begin{aligned}
\sigma_{2D} &= \lim_{R \rightarrow \infty} 2\pi R \frac{|\vec{E}_{t,m}^s|^2}{|\vec{E}^i|^2} \\
&= \lim_{R \rightarrow \infty} \frac{2\pi R E_o^2 a}{R E_o^2} \frac{1}{2} \\
&= \pi a \\
\sigma_{3D} &\simeq \sigma_{2D} \frac{2\ell_c^2}{\lambda} \\
&\simeq a \ell_c^2 \frac{2\pi}{\lambda}
\end{aligned} \tag{A.14}$$

let $k = \frac{2\pi}{\lambda}$, then

$$\boxed{\sigma_{3D} \simeq k a \ell_c^2} \tag{A.15}$$

A.3.2 \vec{E}_{int}^s RCS Calculation.

$$\begin{aligned}
\left| \vec{E}_{int}^s \right|^2 &= \frac{E_o^2}{R} \frac{(a \cos \theta_i)^2}{R} \\
\sigma_{2D} &= \lim_{R \rightarrow \infty} 2\pi R \frac{\left| \vec{E}_{dB}^s \right|^2}{\left| \vec{E}^i \right|^2} \\
&= \lim_{R \rightarrow \infty} \frac{2\pi R E_o^2}{4R E_o^2} \frac{(a \cos \theta_i)^2}{a \cos \theta_i + \ell} \\
&= \frac{\pi}{2} \frac{(a \cos \theta_i)^2}{a \cos \theta_i + \ell} * 2(\text{double bounce term}) \\
&= \frac{\pi (a \cos \theta_i)^2}{a \cos \theta_i + \ell}
\end{aligned} \tag{A.16}$$

$$\begin{aligned}
\sigma_{3D} &\simeq \sigma_{2D} \frac{2\ell_c^2}{\lambda} \\
&\simeq \frac{2\pi}{\lambda} \frac{(a \cos \theta_i)^2}{a \cos \theta_i + \ell} \ell_c^2
\end{aligned} \tag{A.17}$$

let $k = \frac{2\pi}{\lambda}$ and $\ell = d - 2a \cos \theta_i$, then

$$\boxed{\sigma_{3D} \simeq k \frac{(a \cos \theta_i \ell_c)^2}{a \cos \theta_i + \ell}} \tag{A.18}$$

A.3.3 \vec{E}_{tm}^s RCS Calculation.

$$\begin{aligned}
\sigma_{2D} &= \lim_{R \rightarrow \infty} 2\pi R \frac{\left| \vec{E}_{tm}^s \right|^2}{\left| \vec{E}^i \right|^2} \\
&= 8\pi \left| \frac{a \cos \theta_i}{2\sqrt{a \cos \theta_i + \ell}} e^{jk_o(2a \sin \theta_i - \ell)} - \sqrt{\frac{a}{2}} e^{j2k_o a} \right|^2 \\
\sigma_{3D} &\simeq \sigma_{2D} \frac{2\ell_c^2}{\lambda} \\
&\simeq 8 \frac{2\pi}{\lambda} \ell_c^2 \left| \frac{a \cos \theta_i}{2\sqrt{a \cos \theta_i + \ell}} e^{jk_o(2a \sin \theta_i - \ell)} - \sqrt{\frac{a}{2}} e^{j2k_o a} \right|^2
\end{aligned} \tag{A.19}$$

let $k = \frac{2\pi}{\lambda}$, then

$$\sigma_{3D} \simeq 8k\ell_c^2 \left| \frac{a \cos \theta_i}{2\sqrt{a \cos \theta_i + \ell}} e^{jk_o(2a \sin \theta_i - \ell)} - \sqrt{\frac{a}{2}} e^{j2k_o a} \right|^2 \quad (\text{A.20})$$

Bibliography

1. C. A. Balanis, *Advanced Engineering Electromagnetics*. Wiley, 1989.
2. E. F. Knott, J. F. Shaeffer, and M. T. Tuley, *Radar Cross Section*, 2nd ed. Norwood, MA: Artech House, 1993.
3. J. Berrie and G. Wilson, "Design of target support columns using eps foam," *IEEE Antennas and Propagation Magazine*, vol. 45, no. 1, pp. 198–206, February 2003.
4. I. LaHaie, E. LeBaron, C. Roussi, and K. Quinlan, "Processing techniques for removal of target support contamination," *Antennas and Propagation Society International Symposium*, vol. 1, pp. 488–491, July 1993.
5. J. Burns, E. LeBaron, and G. Fliss, "Characterization of target-pylon interactions in rcs measurements," *Antennas and Propagation Society International Symposium*, vol. 1, pp. 144–147, July 1997.
6. M. I. Skolnik, *Introduction to Radar Systems*, 3rd ed. New York: McGraw-Hill, Inc., 2001.
7. A. Peterson, S. Ray, and R. Mittra, *Computational Methods for Electromagnetics*. Oxford University Press, 1998.
8. C. Wang, F. Ling, J. Song, and J. Jin, "A fast algorithm for solving cfe of em scattering," *Antennas and Propagation Society*, vol. 4, pp. 2180–2183, July 1999.
9. ———, "Adaptive integral solution of combined field integral equation," *Microwave Opt. Technol. Lett.*, vol. 19, pp. 321–328, 1998.
10. A. Poggio and E. Miller, *Integral Equation Solutions of Three-Dimensional Scattering Problems*. Hemisphere, 1973, ch. 4, pp. 159–264.
11. R. Harrington, *Field Computations by Moment Methods*. New York: Macmillan, 1968.
12. J. M. Putnam, D. D. Car, and J. D. Kotulski, "Parallel CARLOS-3D - an electromagnetic boundary integral method for parallel platforms," *Engineering Analysis with Boundary Elements*, vol. 19, no. 1, pp. 49–55, 1997.
13. J. Putnam, *CARLOS 3D BOR 2D*, version 4.4.0 ed., BOEING, Boeing McDonnell Douglas, Dept 308, St. Louis, 2000.
14. S. Rao, D. Wilton, and A. Glisson, "Electromagnetic scattering by surfaces of arbitrary shape," *IEEE Transactions on Antennas and Propagation*, vol. AP-30, pp. 409–418, May 1982.
15. A. D. Group, *ACAD User's Manual*, version 9.4 ed., Lockheed Martin Aeronautics Company, P.O. Box 748, Fort Worth, Texas 76101.

Vita

Second Lieutenant Donald W. Powers graduated from Butler High School in Louisville, Kentucky. He entered undergraduate studies at the University of Louisville in Louisville, Kentucky where he graduated with highest honors (Summa Cum Laude). He completed his Bachelor of Science degree in Electrical Engineering in June 2002 and was commissioned through Detachment 295 AFROTC at the University of Louisville.

His first assignment was at Wright-Patterson Air Force Base as an Electrical Engineering student at the Air Force Institute of Technologys Graduate School of Engineering and Management. Upon graduation, he will be assigned to the Air Force Research Lab Signatures Branch.

Permanent address: 2950 Hobson Way
WPAFB, OH 45433

REPORT DOCUMENTATION PAGE				Form Approved OMB No. 074-0188	
<p>The public reporting burden for this collection of information is estimated to average 1 hour per response, including the time for reviewing instructions, searching existing data sources, gathering and maintaining the data needed, and completing and reviewing the collection of information. Send comments regarding this burden estimate or any other aspect of the collection of information, including suggestions for reducing this burden to Department of Defense, Washington Headquarters Services, Directorate for Information Operations and Reports (0704-0188), 1215 Jefferson Davis Highway, Suite 1204, Arlington, VA 22202-4302. Respondents should be aware that notwithstanding any other provision of law, no person shall be subject to a penalty for failing to comply with a collection of information if it does not display a currently valid OMB control number.</p> <p>PLEASE DO NOT RETURN YOUR FORM TO THE ABOVE ADDRESS.</p>					
1. REPORT DATE (DD-MM-YYYY) 23-03-2004		2. REPORT TYPE Master's Thesis		3. DATES COVERED (From – To) Aug 2003 – Mar 2004	
4. TITLE AND SUBTITLE CHARACTERIZATION OF THE TARGET-MOUNT INTERACTION IN RADAR CROSS SECTION MEASUREMENT CALIBRATIONS				5a. CONTRACT NUMBER	
				5b. GRANT NUMBER	
				5c. PROGRAM ELEMENT NUMBER	
6. AUTHOR(S) Powers, Donald W., 2d Lt, USAF				5d. PROJECT NUMBER	
				5e. TASK NUMBER	
				5f. WORK UNIT NUMBER	
7. PERFORMING ORGANIZATION NAMES(S) AND ADDRESS(S) Air Force Institute of Technology Graduate School of Engineering and Management (AFIT/EN) 2950 Hobson Way Street, Building 640 WPAFB OH 45433-7765				8. PERFORMING ORGANIZATION REPORT NUMBER AFIT/GE/ENG/04-21	
9. SPONSORING/MONITORING AGENCY NAME(S) AND ADDRESS(ES) AFRL/SNS Attn: Dr. Kueichien Hill 2591 K St. WPAFB OH 45433-7602 COMM: 937-255-0675 e-mail: kueichien.hill@wpafb.af.mil				10. SPONSOR/MONITOR'S ACRONYM(S)	
				11. SPONSOR/MONITOR'S REPORT NUMBER(S)	
12. DISTRIBUTION/AVAILABILITY STATEMENT APPROVED FOR PUBLIC RELEASE; DISTRIBUTION UNLIMITED.					
13. SUPPLEMENTARY NOTES					
14. ABSTRACT Radar Cross Section (RCS) measurements are quintessential in understanding target scattering phenomenon. The reduced RCS of modern weapons systems stresses the capability of current RCS measurement ranges. A limiting factor that has recently become more significant is the electromagnetic coupling between a test target and the mounting hardware used to support it and control its orientation during the RCS measurement. Equally important is the electromagnetic coupling between the RCS calibration artifact and its mount, which provides an opportunity to explore the coupling phenomena without delving into operationally sensitive areas. The primary research goal was to characterize the interaction between a calibration artifact and its mounting apparatus when measuring the RCS of the calibration artifact as part of a larger RCS measurement process. Standard methods, such as vector background subtraction, do not account for this interaction. By understanding the interaction term, a more accurate measurement of target RCS may be obtained. Through careful characterization of the interaction, an additional term can be included in the vector background subtraction equation to reduce the level of uncertainty. Two techniques were developed to isolate and characterize the interaction between the target and mount. The first involves evaluating the far-zone fields scattered by the target under two conditions: the target alone and then the target with mounting hardware present. The fields are then coherently subtracted to isolate the interaction. This process was validated with measurements and computational results. The second technique involves evaluating fields on the target surface under the aforementioned conditions, which are subsequently subtracted from one another and radiated to the far-field. The advantages and disadvantages of each technique are investigated. Results for twin-cylinder and cylinder/pylon configurations are presented. Validation is achieved through comparison with physical measurements. Results indicate the target-mount interaction is most significant at low frequencies.					
15. SUBJECT TERMS Electromagnetic Scattering, Integral Equations, Method of Moments, RADAR, Stealth Technology, RCS Measurements					
16. SECURITY CLASSIFICATION OF:			17. LIMITATION OF ABSTRACT	18. NUMBER OF PAGES	19a. NAME OF RESPONSIBLE PERSON
a. REPORT	b. ABSTRACT	c. THIS PAGE			Michael J. Havrilla, Ph. D. (ENG)
U	U	U	UU	96	19b. TELEPHONE NUMBER (Include area code) (937) 255-3636, ext 4582; e-mail: Michael.Havrilla@afit.edu